Retrieval of aerosol optical depth and surface reflectance over land from NOAA AVHRR data

Yingjie Li [a,h,i], Yong Xue [a,b,*], Gerrit de Leeuw [c,d,e], Chi Li [f,h], Leiku Yang [g], Tingting Hou [f,h], Farhi Marir [b]

[a] State Key Laboratory of Remote Sensing Science, Jointly Sponsored by the Institute of Remote Sensing Applications of Chinese Academy of Sciences and Beijing Normal University, Beijing 100101, China
[b] Faculty of Life Sciences and Computing, London Metropolitan University, London N7 8DB, UK
[c] Department of Physics, University of Helsinki, Helsinki, Finland
[d] Finnish Meteorological Institute, Climate Change Unit, Helsinki, Finland
[e] Netherlands Organisation for Applied Scientific Research TNO, Utrecht, The Netherlands
[f] Center for Earth Observation and Digital Earth of Chinese Academy of Sciences, Beijing 100094, China
[g] School of Geography, Beijing Normal University, Beijing 100875, China
[h] University of the Chinese Academy of Sciences, Beijing 100049, China
[i] College of Global Change and Earth System Science, Beijing Normal University, Beijing 100875, China

ARTICLE INFO

ABSTRACT

An algorithm for the land aerosol and bidirectional reflectance inversion by times series technique (LABITS) is proposed and applied to data from the National Oceanic and Atmospheric Administration (NOAA) advanced very high resolution radiometer (AVHRR). The surface reflectance and aerosol optical depth are inverted from AVHRR Channel 1 data using a model for the earth-atmosphere system which couples an atmospheric radiative transfer model with the Ross–Thick–Li-sparse bidirectional reflectance factor (BRF) model. Basic assumptions are that the surface bidirectional reflective property does not vary over a 2–4 day periods and that the aerosol characteristics are uniform within a $0.1° \times 0.1°$ window (approximately 10 km × 10 km). The LABITS algorithm is applied to data from AVHRR on the NOAA-15, NOAA-16, and NOAA-18 satellites over four distinct areas, namely, North America, Europe, the Sahara and India, to simultaneously retrieve the aerosol optical depth (AOD), BRF parameters and surface albedo. Preliminary results show that AOD and reflectance retrieved from the three different instruments are in good agreement and that LABITS provides good results over both bright surfaces, e.g. the Sahara, and dark surfaces, e.g. Europe. Evaluation of the AOD versus data from the Aerosol Robotic Network (AERONET) provides a correlation coefficient R^2 of 0.88 and a root-mean-square error (RMSE) of approximately 0.07; and the uncertainty is approximately $\Delta\tau = \pm 0.05 \pm 0.20\tau$. Comparing our results with the moderate resolution imaging spectroradiometer (MODIS) AOD products, over many areas, provides biases in the range of ± 0.05. The surface albedo values calculated from the retrieved BRF parameters are similar to those provided by the MODIS albedo product (MCD43). The robustness and applicability of the LABITS algorithm are demonstrated with the retrieval of AOD over China during August 2008. Daily and monthly averaged results show good agreement with collocated AERONET observations and AQUA MODIS products (MYD04 and MYD08). The AOD uncertainty is estimated as $\Delta\tau = \pm 0.05 \pm 0.30\tau$. The preliminary analysis of time series over selected AERONET sites shows that the temporal variations of the AOD values retrieved by application of LABITS to AVHRR data are overall similar to temporal variations of AOD provided by the MODIS and AERONET. The algorithm has the potential to retrieve global AOD over land for long time series of NOAA AVHRR data going back to the 1980s, which are urgently needed for studies on aerosol climatology and global climate change.

© 2013 Elsevier Inc. All rights reserved.

1. Introduction

Atmospheric aerosols play an important role in global climate change and they can have large health impacts (IPCC, 2007; Lee, 2011; Li et al., 2011; Stedman, 2004; Wilson et al., 1972). Satellite remote sensing provides an effective method for monitoring the spatial distribution and temporal variation of aerosols and, thus, provides a tool to estimate their effects. However, satellite aerosol retrieval over land is difficult because of the problems associated with discriminating between signals measured by a satellite at the top of the atmosphere (TOA) from the earth's surface and from atmospheric aerosols (Kaufman et al., 1997a; Kokhanovsky & de Leeuw, 2009). To retrieve aerosol over land,

Kaufman and Sendra (1988) proposed an algorithm for automatic atmospheric corrections to visible and near-infrared satellite imagery. In this algorithm, AOD over dark dense vegetation (DDV) can be retrieved based on discriminating between land and aerosol reflectance using measurements together with statistical methods. Since its development, the DDV algorithm has become the most common algorithm for aerosol retrieval over land from satellite data. It has been upgraded as a "dark target" and has also become the main algorithm for aerosol retrieval over land using data from the Moderate Resolution Imaging Spectroradiometer (MODIS) (Kaufman et al., 1997b; Levy et al., 2007a,b). A similar algorithm has also been applied to data from the Sea-viewing Wide Field-of-view Sensor (SeaWiFS) and the MEdium Resolution Imaging Spectrometer (MERIS) (von Hoyningen-Huene et al., 2003, 2011). For aerosol retrieval over bright land surfaces, there are three main algorithms: structure function (Tanré et al., 1988), composite background reflectance (Knapp et al., 2002, 2005) and deep blue (Hsu et al., 2004, 2006). These algorithms are based on the assumption that, during a given period of time, the surface properties (structure and reflectance) do not change significantly and can be estimated by the clearest or darkest pixels. Lyapustin et al. (2011a,b) proposed an algorithm called MAIAC (Multi-Angle Implementation of Atmospheric Correction) to retrieve AOD and surface Bidirectional Reflectance Factor (BRF) parameters over land. In MAIAC, the aerosol characteristics over an area of 25×25 pixels (25 km $\times$ 25 km) are assumed to be invariable. Emili et al. (2011) obtained high resolution (1 km $\times$ 1 km) AOD over mountain regions from MODIS data using 1 km $\times$ 1 km BRF parameters to account for surface reflectance. For dual-view and multi-view sensors, such as the Advanced Along-Track Scanning Radiometer (AATSR), the Multi-angle Imaging SpectroRadiometer (MISR) and POLarization and Directionality of the earth's reflectance (POLDER), it is possible to retrieve AOD and surface reflectance simultaneously (Deuzé et al., 2001; Diner et al., 1998, 2005; Veefkind et al., 1998).

For the Advanced Very High Resolution Radiometer (AVHRR), flying on a series of NOAA satellites, Holben et al. (1992) acquired AOD using DDV and structure function algorithms. Xue and Cracknell (1995) proposed the retrieval of surface reflectance from satellite radiance measurements based on a solution of the radiative transfer equation. This approach can be used with NOAA satellite AVHRR data by assuming that the distribution of the aerosol does not vary too rapidly as a function of time. It is usually better to select the AVHRR data from around noon and at dusk on the same day. This approach requires the visibility of the area to be more than 5 km for multiple solar zenith angle observations applications. Soufflet et al. (1997), Molineaux et al. (1998) and Asakuma et al. (2002) also retrieved AOD over dark surfaces using advanced dark-target algorithms. Hauser et al. (2005b) proposed an algorithm for aerosol retrieval over land from AVHRR data. In this algorithm, land surface BRFs are determined by searching the clearest pixels during 45-day time series data. The AOD over Central Europe was derived with a 25 km $\times$ 25 km resolution and compared with MODIS and Aerosol Robotic Network (AERONET) data (Hauser et al., 2005a). Riffler et al. (2010) modified the algorithm by employing a new scheme to determine the surface reflectance.

In this paper, an algorithm for the Land Aerosol and Bidirectional reflectance Inversion by Time Series technique (LABITS) is presented and applied to NOAA AVHRR Channel 1 (Ch.1) data. The results are then validated by comparison with AERONET data. The algorithm is described in Section 2, and the results and comparisons are presented in Section 3. In Section 4, we discuss the advantages and disadvantages of the algorithm and draw conclusions about our work.

2. Methodology

2.1. LABITS algorithm

The principal difficulty of aerosol retrieval from satellite data is the decoupling of the earth-atmosphere system, in which the estimation of the surface reflectance is crucial. Traditional algorithms, such as DDV and deep blue for MODIS data, require the surface reflectance to be determined in advance. In this paper, we develop a new algorithm to jointly retrieve the surface reflectance and aerosol optical depth based on two fundamental assumptions: (1) the surface reflective property changes little during the observation period; and (2) the aerosol optical properties change little over short distances. Therefore, if we use the Ross-Li BRF model, there are only three free parameters describing the surface reflectance during multiple observations, and if we define the elementary processing area as a block with the size of N, there are $N \times N$ pixels with the same AOD and other optical parameters for a single measurement. Except for AOD, the atmospheric parameters can be determined in advance based on prior knowledge (e.g., from ground-based measurements or satellite remote sensing products). Thus, during multiple observations, with the number K representing the block of $N \times N$ pixels and using one single optical channel for retrieval, there are KN^2 measurements and $K + 3 N^2$ unknowns. If

$$KN^2 \geq K + 3N^2 \tag{1}$$

then the number of measurements exceeds the number of unknowns, and we can jointly retrieve the surface BRF and AOD. A similar idea is also used in aerosol retrieval from multi-angle satellite data such as MODIS (Lyapustin et al., 2011a,b), MSG SEVIRI (Carrer et al., 2010; Govaerts et al., 2010; Wagner et al., 2010), and GOES (Zhang et al., 2011). Obviously, in Eq. (1), $K = 4$ and $N = 2$ can meet the requirements, and there are 16 measurements and 16 unknowns. The details of the atmospheric radiative transfer (RT) model and surface bidirectional reflectance distribution function model used to achieve this are presented below.

2.2. Atmospheric radiative transfer model

In the implementation of the LABITS algorithm, an analytical model coupling an atmospheric radiative transfer model and a land surface BRF is used as explained below. The atmospheric RT model uses the following symbols and definitions. Upward and downward radiation are indicated by a positive sign (+) and a negative sign (−), respectively. Based on this definition, the solar zenith angle, θ_s, varies from −90° to −180° and its cosine, $\mu_s = \cos(\theta_s)$, varies in the range [−1, 0]. However, in many calculations, we need a positive value of μ_s, so we must denote the absolute value of μ_s, given as $|\mu_s|$. Other major symbols used herein are listed in Table 1 or are described in the text.

2.2.1. Gas absorption correction

Atmospheric extinction effects include absorption and scattering. Absorption in the visible and near-infrared channels is mainly due to water vapor, ozone and some other trace gases and sometimes aerosols. Scattering is mainly caused by gaseous molecules and aerosols. To separate the contribution of aerosols from other effects, we must correct for the absorption effects of water vapor and ozone. Using Beer's Law, for satellite observations at the top of the atmosphere (TOA), we have

$$F'_0 = F_0 T_g(\mu_s, \mu_v) = F_0 \exp\left[-(\tau_w + \tau_o)\left(\left|\mu_s^{-1}\right| + \mu_v^{-1}\right)\right]. \tag{2}$$

If we define the air mass factor, G, as

$$G = \left|\mu_s^{-1}\right| + \mu_v^{-1} \tag{3}$$

we have

$$T_g(\mu_s, \mu_v) = \exp[-(\tau_w + \tau_o)G]. \tag{4}$$

Table 1
Notations.

Symbol	Description
θ	Zenith angle; the subscripts s and v stand for solar and view, respectively
φ	Azimuth angle; the subscripts s and v stand for solar and view, respectively
μ	Cosine of zenith angle θ, $\mu = \cos(\theta)$
Ω	Unit vector of the solid angle with cosine of zenith angle μ and azimuth angle φ
Θ	Scattering angle
f_k	Three parameters of the Ross–Li BRF model, the subscript $k = iso, vol, geo$
H_k	Three albedo kernels of the Ross–Li model, the subscript $k = iso, vol, geo$
K_k	Three BRF kernels of the Ross–Li model, the subscript $k = iso, vol, geo$
ρ	Surface bidirectional reflectance factor
α	Surface albedo, also called the white-sky albedo
ρ^{TOA}	Apparent reflectance at top of atmosphere
F_0	The extra-terrestrial solar radiance in W·m^{-2}·µm^{-1}·sr^{-1}
F'_0	The solar radiance in W·m^{-2}·µm^{-1}·sr^{-1} corrected for water and ozone absorption
T_g	Transmittance of water vapor and ozone
G	Air mass factor
δ	Dirac delta function
τ	Optical depth; the subscripts $0, r, ae, w, o, a$ stand for the total atmospheric column, molecule, aerosol, water vapor, ozone and molecule + aerosol, respectively
ω	Single-scattering albedo
P	Scattering phase function
g	Asymmetry factor
β	Backscattering ratio
λ	Wavelength in µm
$I(\tau, \Omega)$	Radiance in the direction Ω and at optical depth τ
$I(\tau, \mu)$	Radiance integrated by the azimuth angle at the view zenith angle θ, $I(\tau,\mu) = \int_0^{2\pi} I(\tau,\Omega) d\varphi$
$I^{\pm}(\tau)$	Upward ($+$) and downward ($-$) fluxes, $I^{\pm}(\tau,\mu) = \int_0^1 \mu I(\tau,\pm\mu) d\mu$
$I_0(\tau, \Omega)$	Direct radiance
$I_1(\tau, \Omega)$	Single-scattered radiance
$I_M(\tau, \Omega)$	Multiple-scattered radiance
$I_1^+(\tau)$	Total diffuse upward flux
$I_1^+(\tau)$	Single-scattered upward radiance
$I_M^+(\tau)$	Multiple-scattered upward radiance
γ_i	Coefficients of two-stream approximate, $i = 1,\ldots,4$

Note: Not all the symbols used are listed in Table 1. Symbols not listed are described in the text.

The optical depth of water vapor, τ_w, and ozone, τ_o, can be estimated by the approximations (Lacis & Hansen, 1974; Leckner, 1978; Liang & Strahler, 1994):

$$\tau_w = \frac{0.2385 K_w(\lambda) C_w}{[1 + 20.07 K_w(\lambda) C_w]^{0.45}} \quad (5)$$

$$\tau_o = 0.03 \exp\left[-277(\lambda - 0.6)^2\right] \quad (6)$$

where $K_w(\lambda)$ (in cm^{-1}) is the spectral absorption coefficient of water vapor, and C_w (in cm) is the amount of precipitable water in the atmospheric path which can be obtained from ground-based measurements or satellite retrievals. The values of $K_w(\lambda)$ and the extraterrestrial solar irradiance (in W·m^{-2}·µm^{-1}·sr^{-1}), πF_0, are given by Bird and Riordan (1986). In the following modeling procedure, we only consider the atmospheric extinctions by molecule scattering and aerosol scattering.

2.2.2. Radiation field decomposition and parameterization

The radiation field can be separated into three parts: (a) direct (not scattered) radiance, $I_0(\tau, \Omega)$; (b) single-scattered radiance, $I_1(\tau, \Omega)$; and (c) multiple-scattered, $I_M(\tau, \Omega)$. Each of these parts is individually parameterized:

For direct and single-scattered radiance observed by satellite sensors at the TOA ($\tau = 0$), we have

$$I_0(0, \Omega_v) = F'_0 |\mu_s| \rho(\theta_s, \theta_v, \varphi_s - \varphi_v) \exp(-\tau_a G) \quad (7)$$

$$I_1(0, \Omega_v) = \frac{F'_0 |\mu_s| \omega_a P_a(\Theta)}{4(|\mu_s| + \mu_v)} [1 - \exp(-\tau_a G)] \quad (8)$$

where Θ is the scattering angle defined as

$$\cos(\Theta) = \mu_s \mu_v + \sqrt{(1 - \mu_s^2)(1 - \mu_v^2)} \cos(\varphi_s - \varphi_v). \quad (9)$$

The single scattering albedo (SSA), ω_a; scattering phase function, P_a; and the asymmetry factor (ASYM), g_a, are calculated by optical depth weighting:

$$\omega_a = \frac{\tau_r \omega_r + \tau_{ae} \omega_{ae}}{\tau_r + \tau_{ae}} \quad (10)$$

$$P_a(\Theta) = \frac{\tau_r P_r(\Theta) + \tau_{ae} P_{ae}(\Theta)}{\tau_r + \tau_{ae}} \quad (11)$$

$$g_a = \frac{\tau_r g_r + \tau_{ae} g_{ae}}{\tau_r + \tau_{ae}}. \quad (12)$$

For molecular scattering, we have $\tau_r = 0.00864 \lambda^{-(3.916 + 0.074\lambda + 0.05/\lambda)}$, $\omega_r = 1, g_r = 0$ and $P_r(\Theta) = 0.75[1 + \cos^2(\Theta)]$. Polarization is not taken into account (Liang, 2000; Liang & Strahler, 1994). For aerosol scattering, the optical parameters are determined by aerosol composition and size, and the phase function can be estimated by a one-term Henyey–Greenstein function (H–G function) (Henyey & Greenstein, 1941):

$$P_{ae}(\Theta) = P_{H-G}(\Theta) = \frac{1 - g_{ae}^2}{[1 + g_{ae}^2 - 2g_{ae} \cos(\Theta)]^{1.5}}. \quad (13)$$

The H–G function is a rough approximation of a real aerosol scattering phase function and is commonly utilized in some retrieval algorithms to describe the aerosol scattering matrix (Carrer et al., 2010; Seidel et al., 2010). Also it is also used in some land surface radiative transfer models such as models by Hapke (1981), Rahman et al. (1993) and Verstraete et al. (1990). It is selected for use in our forward model for simplicity. However, in certain circumstances this assumption can lead to considerable retrieval uncertainties. This issue will be discussed later.

For multiple-scattered radiance, a two-stream approximation is employed. Meador and Weaver (1980) have shown that an entire class of approximate two-stream solutions can be reduced to a standard form with only a few coefficients:

$$\begin{cases} \dfrac{dI^+(\tau)}{d\tau} = \gamma_1 I^+(\tau) - \gamma_2 I^-(\tau) - \pi F'_0 \omega_a \gamma_3 \exp\left(-\dfrac{\tau}{|\mu_s|}\right) \\ \dfrac{dI^-(\tau)}{d\tau} = \gamma_2 I^+(\tau) - \gamma_1 I^-(\tau) + \pi F'_0 \omega_a \gamma_4 \exp\left(-\dfrac{\tau}{|\mu_s|}\right) \end{cases} \quad (14)$$

where $I^{\pm}(\tau)$ stand for upward and downward fluxes and $\gamma_1, \gamma_2, \gamma_3$ and γ_4 are the coefficients. Here, we use the hybrid modified Eddington-delta approximation, which has been proven generally superior to other two-stream approximations over a wide range of atmospheric conditions (Joseph & Wiscombe, 1976; Liang & Strahler, 1993). More details about the multiple-scattered radiance estimation are provided in Appendix A.

Based on the equations above, the apparent reflectance at the TOA observed by satellite sensors, including gaseous absorption and the direct, single-scattered and multiple-scattered components, ρ^{TOA} can be written as

$$\rho^{TOA} = \frac{T_g(\mu_s, \mu_v)[I_0(0, \Omega_v) + I_1(0, \Omega_v) + I_M(0, \Omega_v)]}{|\mu_s| F_0}$$
$$= e^{-(\tau_w + \tau_o)G} \cdot \left[\rho(\theta_s, \theta_v, \varphi_s - \varphi_v) \exp(-\tau_a G) + \frac{\omega_a P_a(\Theta)\left(1 - e^{-\tau_a G}\right)}{4(|\mu_s| + \mu_v)} + \frac{I_M(0, \Omega_v)}{F_0 |\mu_s|} \right]. \quad (15)$$

2.3. Surface BRF/albedo model

For surface BRF, we employ a semi-empirical model, the Ross–Thick–Li-Sparse model, also simply referred to as the Ross–Li BRF model, which is the standard model used in MODIS Bidirectional Reflectance Distribution Function (BRDF) processing (Schaaf et al., 2002). The basic assumption of the Ross–Li BRF model is that the land surface reflectance can be modeled as the sum of three kernels representing basic scattering types: isotropic scattering; radiative transfer type volumetric scattering, such as from horizontally homogeneous leaf canopies; and geometric-optical surface scattering, such as from scenes containing three-dimensional objects that cast shadows and are mutually obscured from view at off-nadir angles (Strahler & Muller, 1999). The Ross–Li BRF model is expressed as (Wanner et al., 1995)

$$\rho(\theta_s, \theta_v, \varphi_s - \varphi_v) = f_{iso}K_{iso} + f_{vol}K_{vol} + f_{geo}K_{geo}. \qquad (16)$$

The expressions for all three kernels can be found in Appendix B.

After obtaining the BRF, the albedo, which is also termed the white-sky albedo in the MODIS product, can be calculated by integration. Similar to the BRF, we have the following polynomial expression (Strahler & Muller, 1999)

$$\alpha = f_{iso}H_{iso} + f_{vol}H_{vol} + f_{geo}H_{geo} \qquad (17)$$

where $H_{iso} = 1$, $H_{vol} = 0.189184$ and $H_{geo} = -1.377622$.

2.4. Data processing

In this work we use data from two AVHRR instruments which reduces the revisit period to approximately 0.5–1 day. Consequently, 2–4 days of observations in cloud-free conditions (a condition to be able to do aerosol retrieval) will provide sufficient observations for BRF and AOD retrieval. The NOAA AVHRR processing steps are as follows:

(1) Preprocess NOAA AVHRR Level 1B data. Preprocessing includes calibration, cloud masking, gas absorption correction, geo-referencing and region of interest (ROI) selection. In our study, the calibration coefficients and the navigation data (latitude, longitude, solar zenith angle, view zenith angle, and relative azimuth angle) are obtained from NOAA AVHRR Level 1B data. The details of the calibration or calculation of top-of-atmospheric reflectance can be found in the NOAA KLM user's guide with the NOAA-N, -N′ supplement (Robel, 2009). The cloud mask is based on the CLAVR (Clouds from AVHRR) algorithm (Stowe et al., 1991, 1999). For the correction for gas absorption, the amount of precipitable water is obtained from MODIS Level 3 daily atmospheric products and the optical depth of ozone is given by Eq. (6) as approximately 0.0234 for the center wavelength of AVHRR Ch.1 at 0.63 μm. The images are re-projected with a geographic longitude/latitude projection and with the WGS-84 coordinate system. The resolution is resized to $0.05° \times 0.05°$.

(2) Estimate the aerosol scattering parameters, including aerosol SSA and ASYM from ground-based measurements if available, such as AERONET Level 2.0 almucantar inversion data (Dubovik & King, 2000; Dubovik et al., 2000), or from a climatology for the ROIs. To determine aerosol scattering parameters from AERONET data, the SSA and ASYM are calculated by Mie scattering theory (Mie, 1908). If ground-based measurements are not available, the MODIS global aerosol classification and parameterization from the climatology are applied (http://modis.gsfc.nasa.gov/data/dataprod/dataproducts.php?MOD_NUMBER=04). In the MODIS Collection 5 (C005) algorithm, global aerosols are divided into three fine modes: non-absorbing, moderately absorbing, absorbing, and one coarse model, dust. Each model includes two modes, an accumulation mode (one of the three fine mode
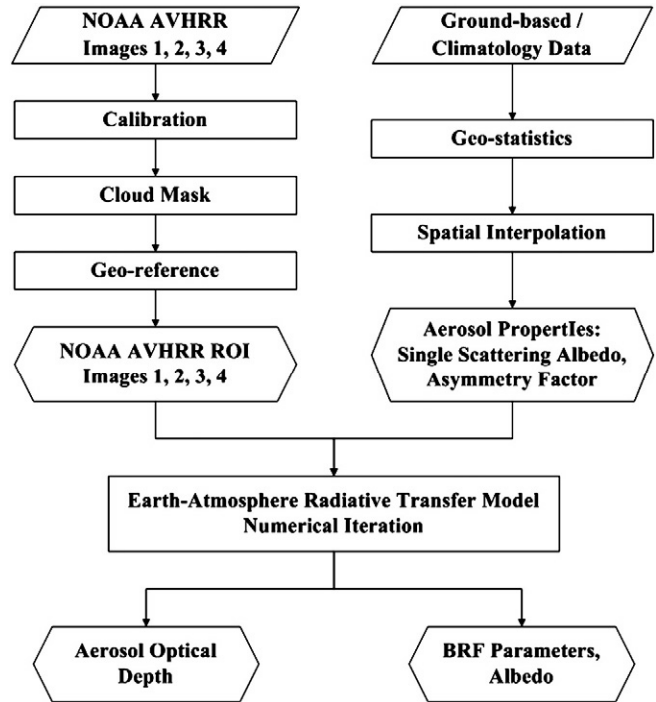

Fig. 1. Flowchart of the LABITS algorithm.

models) and a coarse mode. The fine mode fraction (FMF) can be obtained from the MODIS aerosol product (Levy et al., 2007a,b).

(3) Solve the nonlinear equations to obtain the AOD and BRF parameters jointly. In the implementation of the LABITS algorithm, a numerical iteration algorithm, Broyden (Press et al., 1992), is used instead of the conventional look-up table (LUT) method, because LUTs are based on a huge bulk of previously computed data, which must be recomputed each time when the atmospheric model is changed (Katsev et al., 2009). In the iteration, the initial values of the AOD and BRF are necessary which are set to the averages for the observation period as determined from long-term MODIS aerosol and BRDF products, respectively.

The flowchart for the AVHRR data processing is shown in Fig. 1.

3. Results and comparison

To test and validate our algorithm, we selected four ROIs, namely AME (Eastern North America), EUR (South Central Europe), SAH (the Sahara) and IND (India), representing typical and distinct surface and aerosol conditions, to retrieve the AOD and BRDF/albedo data and compare the results with ground-based measurements and relevant satellite products. Furthermore, because we are focused on aerosol retrieval over China and aim to obtain the long-term aerosol product to study climate change, we then retrieve AOD over China from NOAA AVHRR data in August 2008. The results are evaluated and analyzed.

Table 2
Regions of interest (ROIs).

ROI Name	Geographic location	Image size	Start (S) and end (E) date (mm/dd/yyyy)	Satellite
AME	90.0 W–70.0 W, 25.0 N–45.0 N	400×400	S: 10/01/2001 E: 10/04/2001	NOAA16
EUR	5.5E–25.5E, 36.0 N–56.0 N	400×400	S: 08/14/2001 E: 08/15/2001	NOAA15 NOAA16
SAH	15.0 W–15.0E, 5.0 N–35.0 N	600×600	S: 04/29/2006 E: 04/30/2006	NOAA16 NOAA18
IND	67.5E–87.5E, 15.0 N–35.0 N	400×400	S: 04/29/2008 E: 05/02/2008	NOAA18

3.1. AOD and BRDF/albedo retrieval over four ROIs

The details of the ROIs, including geographic locations, image sizes, and dates of satellite observation, are shown in Table 2. The NOAA AVHRR RGB images and the AERONET site locations are shown in Fig. 2. Because AVHRR has only two channels in the visible and near-infrared parts of the electro-magnetic spectrum, false color composite images similar to true color composite images, were obtained by setting the RGB channels as: Red — Ch.2, Green — Ch.2 and Blue — Ch.1. Using this color composition, water (ocean and lake) is dark blue, vegetation is green and cloud is white. Fig. 3 shows the land cover for the four selected ROIs as obtained from the MODIS land cover product, MCD12. The classification notations are shown in Table 3.

The selected satellite data for the current study are NOAA-15, NOAA-16, and NOAA-18 AVHRR/3 Level 1B Global Area Coverage (GAC) data. The resolution of the GAC data is 4.36×4.36 km^2, and other characteristics of the GAC data are shown in Table 4. Because for the Ch.2 waveband of AVHRR the absorption effect by water vapor cannot be ignored and may cause the large uncertainties of aerosol inversion, only one channel, Ch.1, is used in our study. The spectral range of Ch.1 is 0.58–0.68 μm, and the central wavelength is approximately 0.63 μm (Robel, 2009).

In our retrieval, the aerosol scattering parameters, SSA and ASYM are estimated from retrieval results from ground-based measurements. The aerosol size distribution and refractive index data from AERONET Level 2.0 almucantar inversion data in each ROI were averaged and SSA and
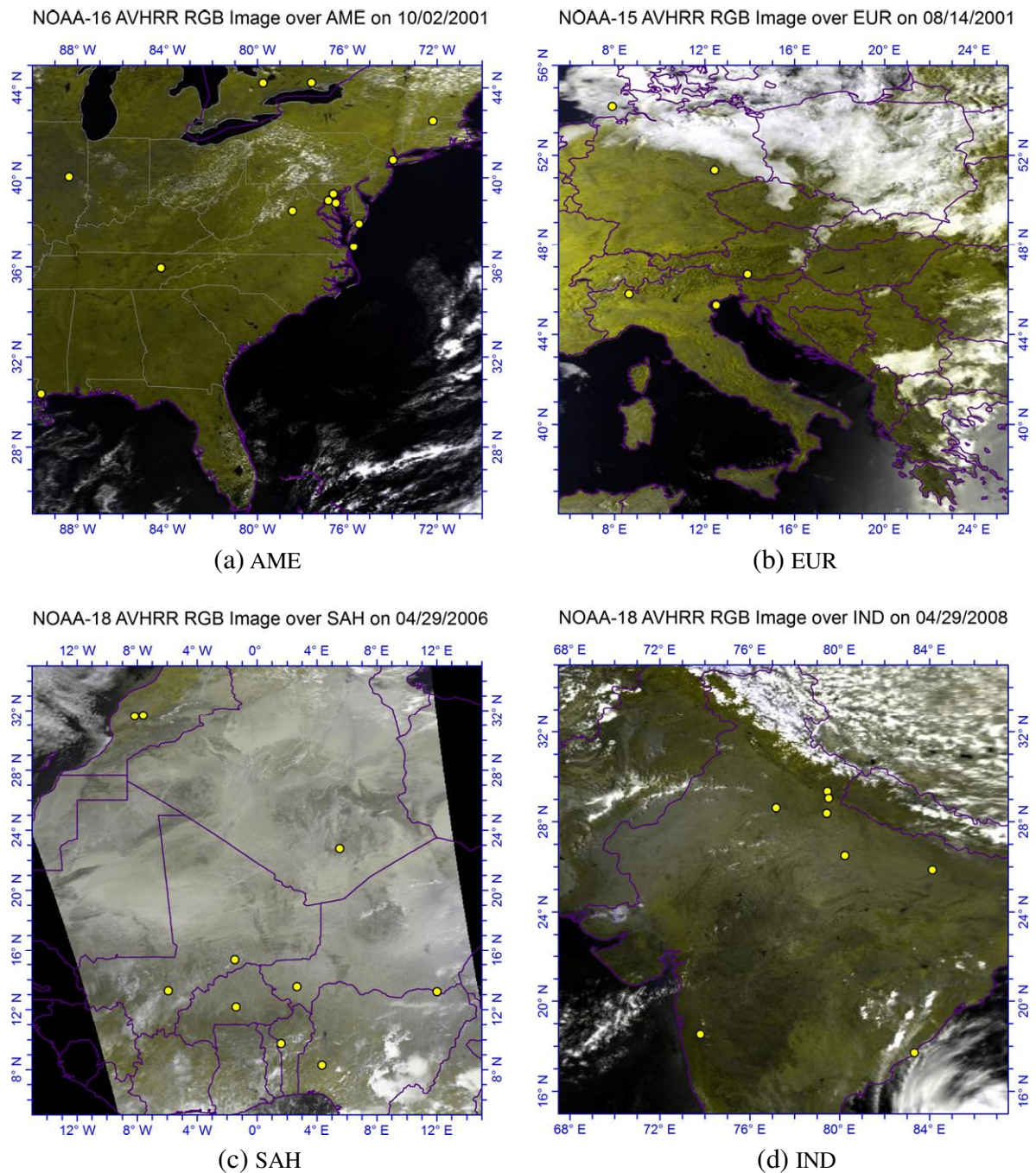

Fig. 2. NOAA AVHRR RGB Images composited by Red: Ch.2, Green: Ch.2 and Blue: Ch.1 and AERONET site locations (yellow spots) over the ROIs. (a) AME (Eastern North America); (b) EUR (South Central Europe); (c) SAH (the Sahara); and (d) IND (India).

ASYM were calculated using Mie scattering theory (Mie, 1908). The averaged aerosol size distributions for each ROI are plotted in Fig. 4. The SSA and ASYM in each ROI are shown in Table 5. It is noted that assigning fixed aerosol properties to a given location based on a long-term average is not appropriate for an operational design because the aerosol characteristics over a site can vary strongly in a few hours especially during events such as dust transport or forest fire (Lee & Kim, 2010; Omar et al., 2005). Thus, in many algorithms, aerosol types are varied. Because this paper focuses on evaluating the use of the retrieval algorithm by application to some cases under different conditions, this issue can be ignored here because we carefully select retrieval cases for which the aerosol intrinsic properties do not vary much. The data in Fig. 4 and Table 5 clearly show the large differences in aerosol optical properties between the four regions. Aerosols in AME and EUR are dominated by fine mode aerosol and EUR has lower SSA values

and thus larger absorption. In contrast, SAH and IND are strongly affected by mineral dust which shows in the stronger coarse-mode. It is noticed that aerosol in IND exhibits more complex and strong absorption, indicative of industrial pollution and dense population, whereas natural dust emission sources are dominant in SAH.

The four-day variation of aerosols can be predicted as minimal in the absence of extreme events, but how the uncertainty of the aerosol type parameters (SSA and g) will affect the signal received by satellite is unknown. Therefore, a brief sensitivity study is conducted to examine this effect. The three kernel coefficients are fixed as $f_{iso} = 0.08$, $f_{vol} = 0.04$ and $f_{geo} = 0.02$; therefore, the white-sky albedo, calculated with Eq. (17), is approximately 0.060. The observing geometry is set as defined in Fig. 5, i.e. $\theta_s = 40°$, $\theta_v = 45°$ or $75°$ and $\Delta\varphi = 50°$. We vary the SSA and g in four areas around their calculated values by ± 5% and compute how TOA reflectance derived from our forward radiative
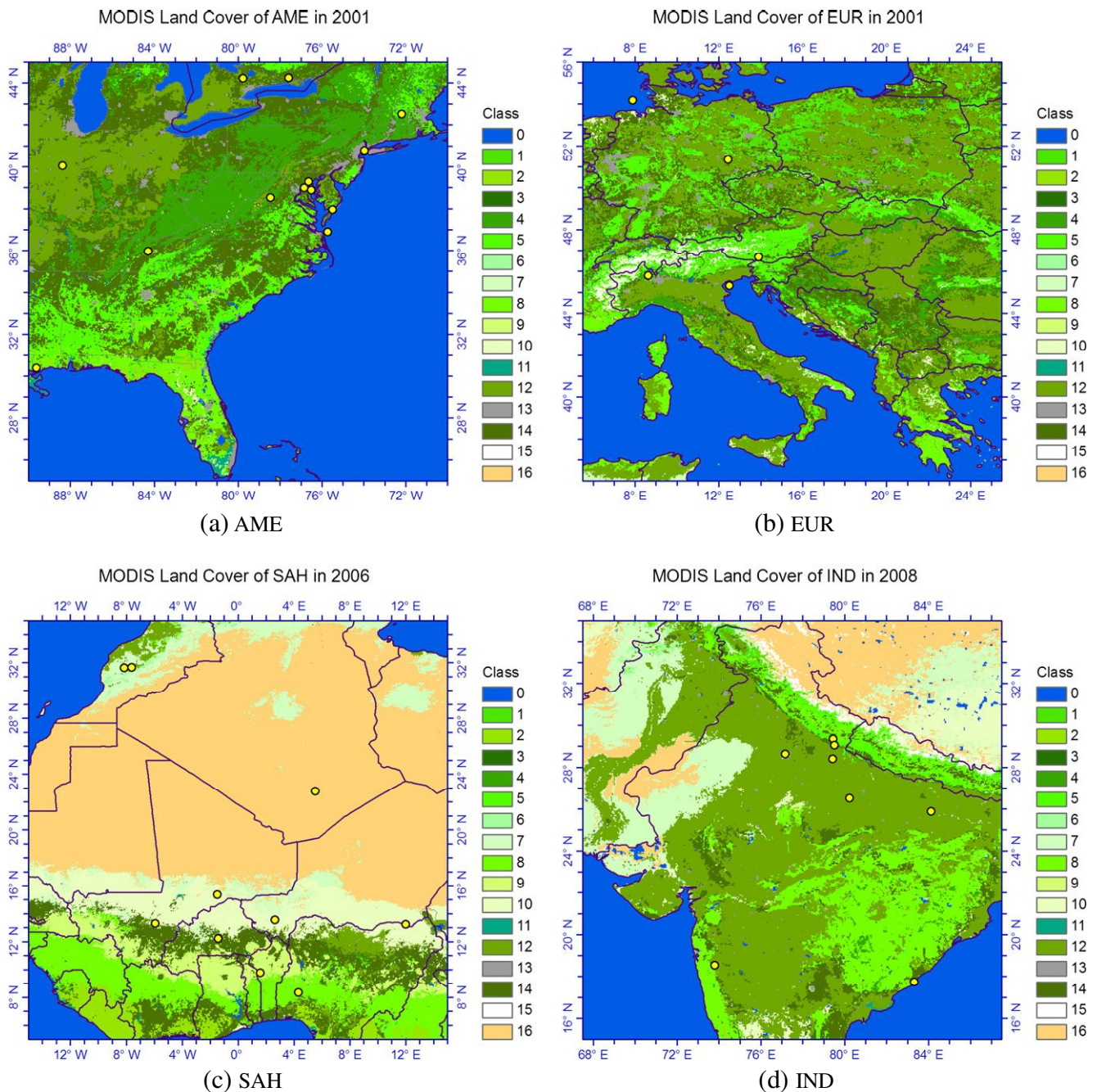

(a) AME

(b) EUR

(c) SAH

(d) IND

Fig. 3. Land cover in the ROIs from MODIS product (MCD12). The yellow spots are AERONET site locations. (a) AME; (b) EUR; (c) SAH; and (d) IND.

Table 3
MODIS land cover classification (Strahler, 1999).

Code	Classification
0	Water bodies
1	Evergreen needleleaf forests
2	Evergreen broadleaf forests
3	Deciduous needleleaf forests
4	Deciduous broadleaf forests
5	Mixed forests
6	Closed shrublands
7	Opened shrublands
8	Woody savannahs
9	Savannahs
10	Grasslands
11	Permanent wetlands
12	Croplands
13	Urban and built-up lands
14	Cropland/natural vegetation mosaics
15	Snow and ice
16	Barren

Fig. 4. Aerosol size distributions over the four ROIs.

transfer model changes for different aerosol loadings. The results in Fig. 5 clearly show that in very low (when the aerosol signal is negligible) and very high AODs (when multiple scattering of light is compensated by absorption) the dependence of the TOA reflectance on AOD is generally weaker than for intermediate AOD values in the range from 0.3 to 1.5. Furthermore, larger zenith angles tend to contribute positively to the sensitivity, especially for low aerosol loadings, by extending the scattering path lengths at smaller scattering angles. Typically, a 5% uncertainty of SSA and g will induce a change of TOA reflectance by 20%, which implies that an accurate estimation of aerosol type parameters is of great importance.

The AOD retrievals by the LABITS algorithm over the ROIs are plotted in Fig. 6. To illustrate the results, we only plot one map for each ROI: NOAA-16 AVHRR AOD map over AME on 10/03/2001, NOAA-15 AVHRR AOD map over EUR on 08/15/2001, NOAA-18 AVHRR AOD map over SAH on 04/29/2006 and NOAA-18 AVHRR AOD map over IND on 04/29/2008. Combining Figs. 3 and 6 we can see that in AME and EUR the major land cover types are vegetation, including forests, croplands, shrubland, and grasslands. The reflectance of this vegetation type in AVHRR Channel 1 is generally very low and thus the surface contribution to the satellite signals is less than that of other land cover types. In addition, the air is clear with low AOD values of less than 0.3. In SAH, most areas are covered by desert and high AOD values are observed which in some places is higher than 1.0 in the presence of dust. In IND, the major land cover types include croplands, woody savannas and shrublands. In some other places, the land is covered by desert. Because of dust emission and heavy industrial pollution, the air quality is usually very poor leading to AOD values exceeding 0.4 in most areas. Some other areas are covered by haze, leading to AOD

values as high as 2.0 are observed. Overall, all areas with consistently high aerosol loadings are distributed along the Indian northeast city corridor with heavy traffic and high population density, stretching from New Deli through Kanpur to Patna.

To evaluate the LABITS algorithm, we also compare the results with MODIS AOD products. MODIS AOD is provided for 0.66 μm whereas the AVHRR Ch1 center is situated at 0.63 μm. However in view of this small difference as well as the differences in bandwidth, with a much wider AVHRR band, the MODIS data are not corrected to 0.63 μm as the difference is neglectable. For AME and EUR, Terra MODIS C005 products are selected and for SAH and IND, Aqua MODIS C051 products are selected which include deep blue results over highly reflecting surfaces. The differences between LABITS AOD and MODIS AOD, i.e., LABITS–MODIS, are plotted in Fig. 6 on the right hand side. The difference maps show that the LABITS-retrieved AOD values are similar to the MODIS products. In AME and EUR, the biases are generally between −0.05 and 0.05. Larger differences usually appear near clouds, at the edge or in the cloud shadow. However, in SAH and IND, the results are less good. In some areas, the biases between LABITS AOD and MODIS AOD are larger than ±0.15, which can be explained as follows. First, Fig. 4 shows that coarse mode aerosols dominant in SAH and IND and are dust and industrial polluted. For these irregular coarse particles, Mie calculations of aerosol optical properties are inaccurate. In other words, the optical properties of the specific aerosol types are not reproduced very well in the RT model we employed. Second, the BRDF/albedo estimations by the Ross-Li model in the ROIs are also inaccurate. In SAH, the dominant land cover is desert, whereas in IND, the land cover is heterogeneous. For these land cover types, the Ross-Li model is not ideal.

In EUR and SAH, the AOD retrievals on the same day, using AVHRR on two different NOAA satellites, are may be somewhat different as shown in Fig. 7 for two days. The differences are due to (1) different observation times correspond to different solar zenith angles and azimuth angles. In some geometric conditions the accuracy of the RT model is sub-par. (2) different atmospheric conditions, especially different aerosol types and concentrations. Fig. 8 shows time series of the AOD and AERONET-retrieved particle size distributions at the Tamanrasset_TMP site, which is located in the middle of the Sahara, on 04/29/2006. (3) each satellite sensor has a distinct SNR (Signal

Table 4
NOAA AVHRR GAC data characteristics (Robel, 2009).

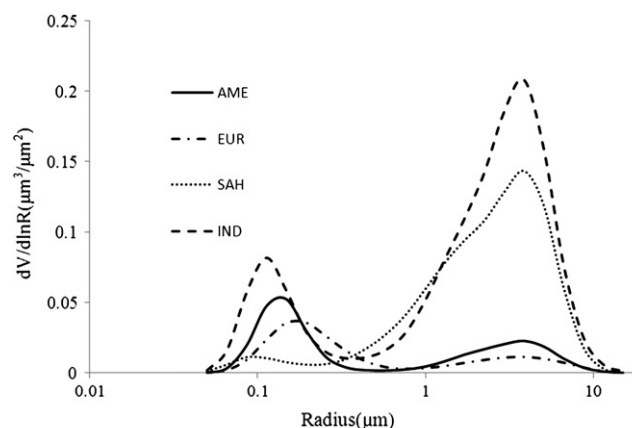| Parameter	Value
Sample word size	10 bits
Number of sampled channels/ available channels	5/6
Number of earth samples per scan	409 per channel
Scan rate	120 scans per minute
Scan direction	East to west (northbound)
Instantaneous Field of View (IFOV)	0.07449° (all channels)
Spatial resolution at nadir	4.36 km (cross track average) by 1.09 km (along track) at 833 km altitude
Cross track distance between sample centers at nadir	5.45 km at 833 km altitude
Along track distance between sample centers at nadir	3.27 km at 833 km altitude
Cross-track scan coverage	±55.4° from nadir
Swath width	2399 km at 833 km altitude

Table 5
Aerosol scattering properties in the four ROIs.

ROI	SSA	ASYM
AME	0.9748	0.5906
EUR	0.9011	0.6650
SAH	0.9241	0.6795
IND	0.8621	0.6315

to Noise Ratio) and SRF (spectrum response function). The SRFs of NOAA-15, -16, and -18 AVHRR Ch.1 can be found in Robel (2009).

A comparison of the LABITS-retrieved AOD with AERONET measurements is presented in Fig. 9 for each ROI and in Fig. 10 for all sites together. Because of the spectral difference between the satellite and AERONET data, we interpolate AERONET AODs to the AVHRR Ch.1 wavelength of 0.63 μm using Eq. (18) (Eck et al., 1999; King & Byrne, 1976)

$$\ln[\tau_{ae}(\lambda)] = a_0 + a_1 \ln(\lambda) + a_2 [\ln(\lambda)]^2 \qquad (18)$$

where a_0, a_1 and a_2 are coefficients and can be obtained from AERONET statistics. The interval between collocated satellite and AERONET measurements is constrained to be less than ± 30 min. Therefore, we assume that during that interval, the AOD does not change.

From Fig. 9, we can see that for all ROIs except in IND, the correlation coefficients R^2 are larger than 0.5 and the root-mean-square errors (RMSE) are less than 0.1. We can also see that in SAH and IND our AOD inversions are somewhat higher than the AERONET AODs, especially when the AERONET AOD > 0.2. In AME and EUR, the retrieved AODs fluctuate around the AERONET data. Fig. 10 shows that for all sites, the number of points is 63, the overall correlation coefficient R^2 is 0.88, the RMSE is 0.07 and the uncertainty for AOD (τ) is $\Delta\tau = \pm 0.05 \pm 0.20\tau$. Overall, from the four cases over AME, EUR, IND and SAH, we can see that for entirely different land cover types and aerosol types, we derive reasonable AOD values ranging from 0.0 to 2.0. Therefore, the LABITS algorithm can be applied for many land surface and aerosol types.

Using the LABITS algorithm, we can jointly retrieve AOD and BRF parameters. Herein, we present the albedos calculated by Eq. (16) for the ROIs. Because of a lack of ground-based validation data, we
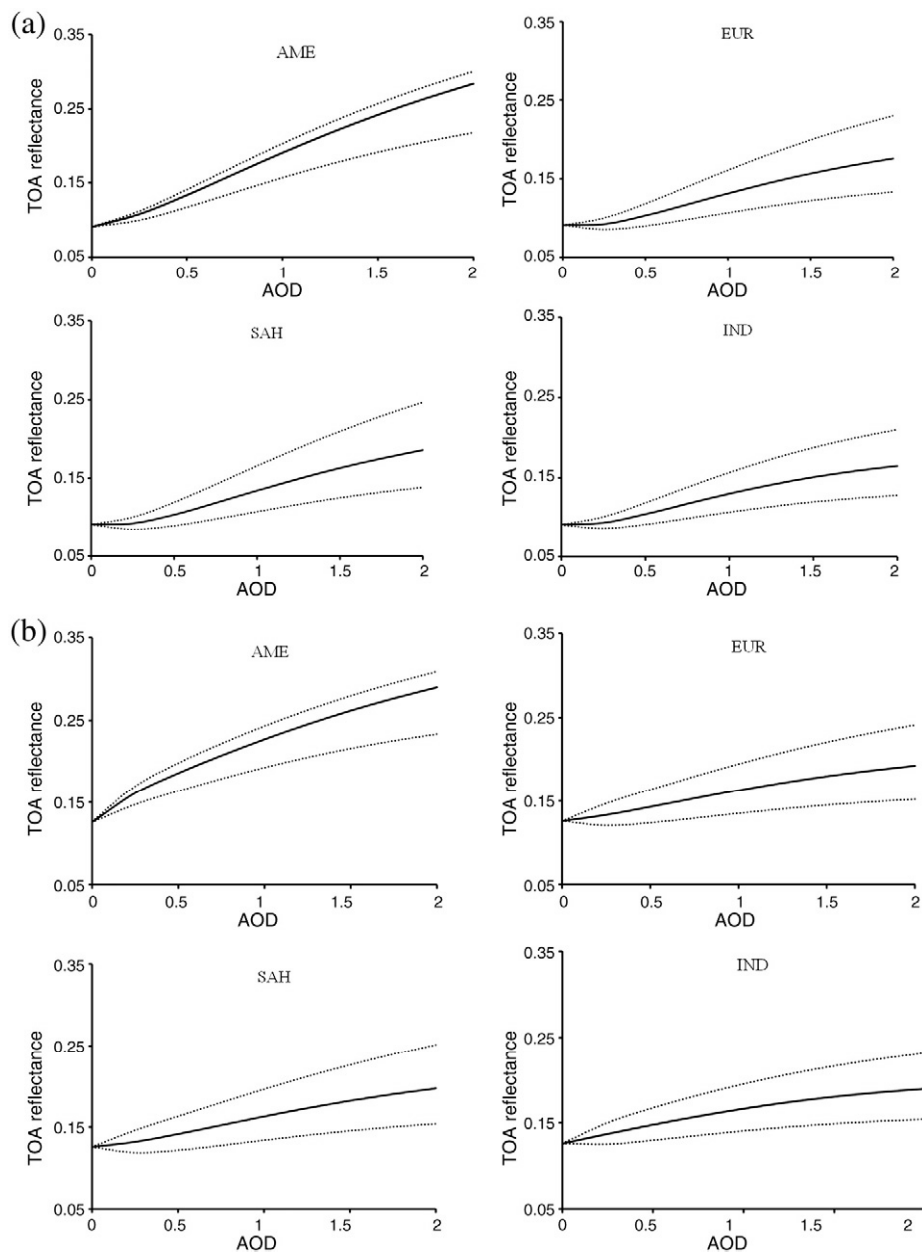

Fig. 5. A brief sensitivity analysis of the RT model. (a) TOA reflectance variation with aerosol loadings in the four ROIs for $\theta_s = 40°$, $\theta_v = 45°$ and $\Delta\varphi = 50°$ (corresponding to an albedo of 0.060 and a BRF of 0.069); dotted lines report the uncertainty envelope induced by a 5% error in SSA and g; (b) Same as (a) but $\theta_v = 75°$ (corresponding to a BRF of 0.072).

assess NOAA AVHRR Ch.1 albedo inversions by comparing them with MODIS Band 1 (0.62–0.67 μm) albedo products (MCD43C3). The LABITS albedos and the difference maps, LABITS – MODIS, are shown in Fig. 11. We can see that the albedos at 0.63 μm over AME and EUR are very low, generally less than 0.1, because the major land cover type is dark dense vegetation. The differences in AME and EUR are between −0.05 and 0.05. In SAH, the desert albedo is much higher, usually above 0.4, and in IND, the albedos vary from 0.1 to 0.5. However, the biases in the two ROIs are large, especially in SAH. As discussed above, in these ROIs, the accuracies of the RT model and the BRF model are not so good, thus the AOD and BRF/albedo retrievals are not as reliable as those in AME and EUR.

From the AOD and the albedo results of the ROIs, we can see that our algorithm performs satisfactorily over dark surfaces, such as the European and American regions, and somewhat less good over bright surfaces, such

as the Saharan and Indian regions. The AOD results over AME and EUR are better than those over SAH and IND. Additionally, for AVHRR datasets onboard different NOAA satellites (i.e., NOAA-15 & NOAA-16 over EUR and NOAA-16 & NOAA-18 over SAH), the retrieval results are generally consistent. The differences are caused by the different observation geometries, atmospheric conditions, and sensor characters.

3.2. AOD mapping over China in August 2008

After testing the LABITS algorithm over different land covers, we apply it to aerosol retrieval over China, which offers a range of complicated atmospheric and surface conditions to verify its applicability and robustness and to discuss its applicability for long-term climate studies. The area covers 70°–140°E, 0°–60°N and the datasets collected include NOAA-18 AVHRR Level 1B GAC data and collocated AERONET data for
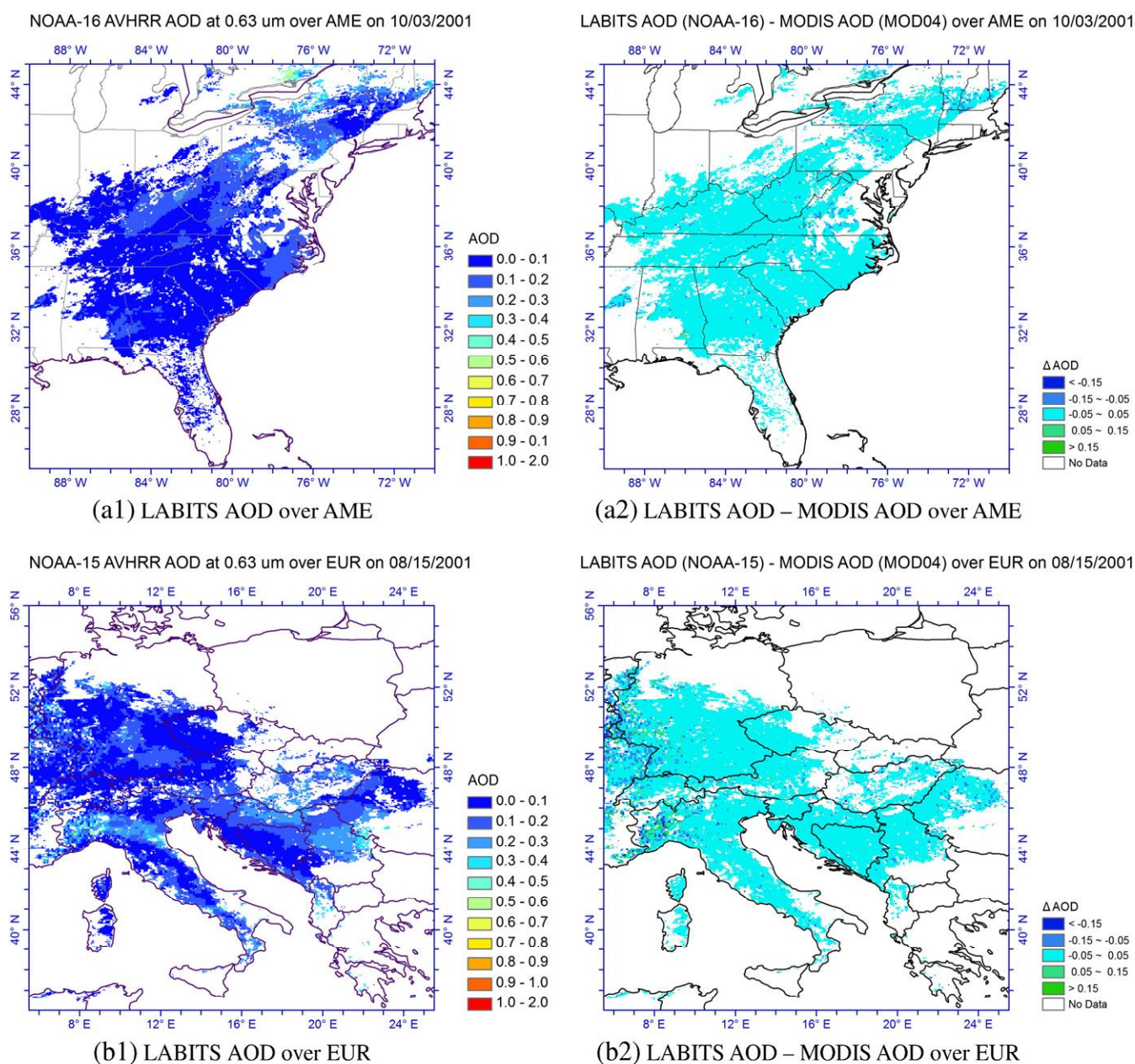

Fig. 6. Retrieved AODs by the LABITS algorithm and the differences between the LABITS and MODIS retrievals over the ROIs. (a1) LABITS AOD over AME; (a2) LABITS AOD–MODIS AOD over AME. (b1) LABITS AOD over EUR; (b2) LABITS AOD–MODIS AOD over EUR; (c1) LABITS AOD over SAH; (c2) LABITS AOD–MODIS AOD over SAH; (d1) LABITS AOD over IND; (d2) LABITS AOD–MODIS AOD over IND.
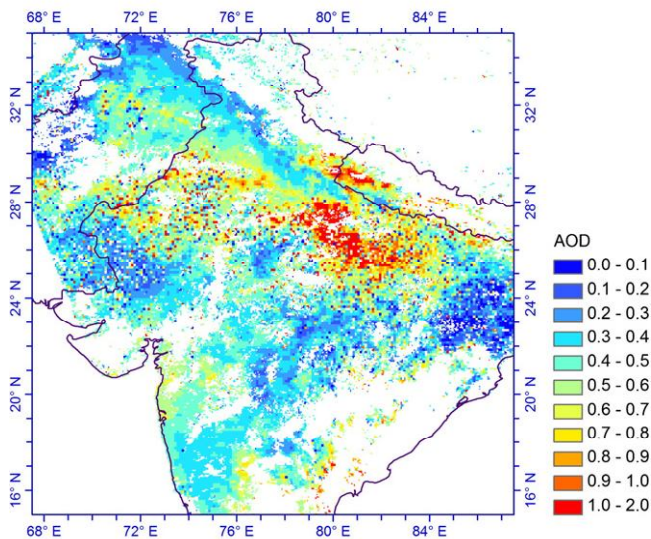
NOAA-18 AVHRR AOD at 0.63 um over SAH on 04/29/2006
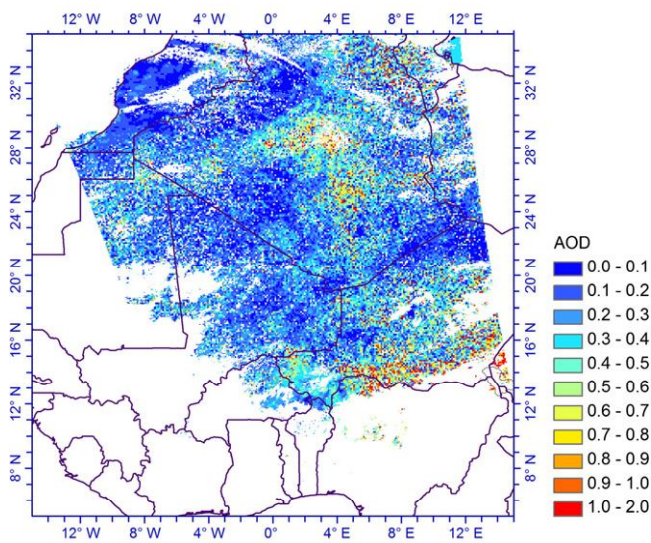
(c1) LABITS AOD over SAH

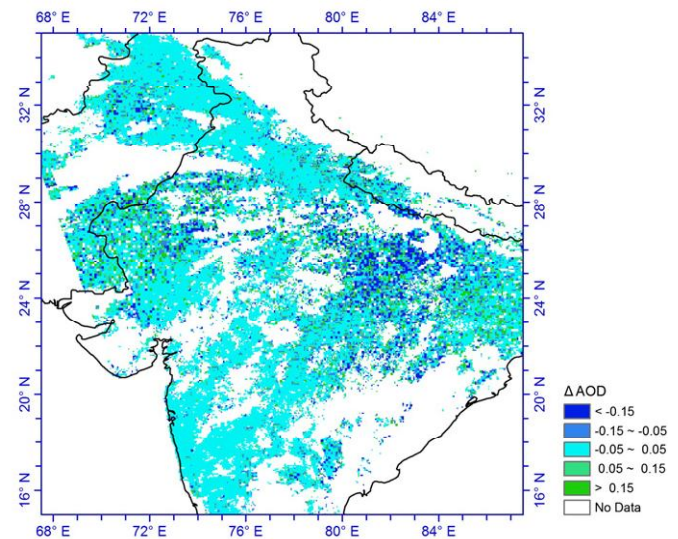LABITS AOD (NOAA-18) - MODIS AOD (MYD04) over SAH on 04/29/2006
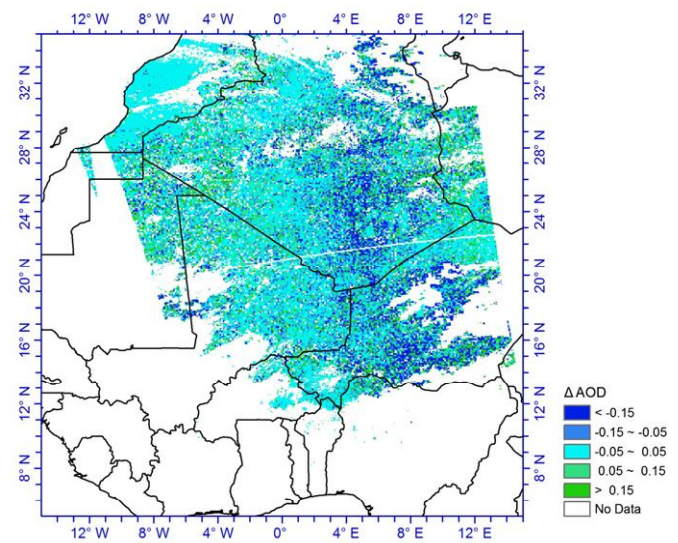
(c2) LABITS AOD – MODIS AOD over SAH

NOAA-18 AVHRR AOD at 0.63 um over IND on 04/29/2008

(d1) LABITS AOD over IND

LABITS AOD (NOAA-18) - MODIS AOD (MYD04) over IND on 04/29/2008

(d2) LABITS AOD – MODIS AOD over IND

Fig. 6 (*continued*).

AOD comparison in August 2008. Fig. 12 shows the study area map and AERONET site locations. Aerosol SSA and ASYM over the area are estimated by using the MODIS global aerosol classification map and parameterization (Levy et al., 2007a). In the MODIS operational algorithm over land, aerosols are comprised of a fine and a coarse mode fraction. In our study, the FMF is obtained from the level-3 MODIS atmosphere monthly global product, MYD08_M3. The spatial distributions of the derived SSA and ASYM over China are shown in Fig. 13. These distributions show an obvious distinction between East China (economically developed areas) and West China (less civilized regions). Overall, aerosols over East China are more polluted and consequently more absorbing so the SSA is smaller than in West China. The ASYM in West China is larger, which means the backscattering ratio is smaller (see Eq. (A3) in Appendix A).

The AVHRR AOD results and MODIS aerosol product for 08/04/2008, including the 'dark target' and 'deep blue' algorithm results, are shown

in Fig. 14. Based on both the AVHRR and MODIS AOD, the AOD at 0.63 μm over many areas is smaller than 0.4, whereas higher values occur over developed regions along China's coast such as the Yangtze River Delta and the Beijing–Tianjin–Hebei region. Another high-AOD-value region in China is the South Xinjiang Basin where the high AOD is due to geographical and meteorological factors. Moreover, the Takli-makan desert, the largest desert in China, is situated in this region and it is one of the sources of dust storms in the Northwest of China. White areas in Fig. 14 indicate the occurrence of clouds (AOD retrieval not possible). Cloudy areas in the MODIS and AVHRR maps are different due to differences in cloud masking. In Fig. 15 monthly averaged AODs for AVHRR and MODIS are shown. Difference maps between the LABITS AVHRR and MODIS products and scatter diagrams for 08/04/2008 as well as for the monthly product are presented in Figs. 16 and 17.

Overall, the aerosol geographical distributions of AVHRR and MODIS results are similar, but there are some differences. In Fig. 16, the

difference between AVHRR and MODIS AODs on 08/04/2008 is small, usually in the range of ± 0.05. There is a high correlation between the daily AVHRR and MODIS AODs. For the day presented here (08/04/2008) $R^2 = 0.75$, RMSE is approximately 0.11 and the regression equation is $\tau_{AVHRR} = 0.93\tau_{MODIS} + 0.02$. However, for the monthly AODs, Fig. 17, the bias is very high. The correlation $R^2 = 0.58$. The regression equation is $\tau_{AVHRR} = 0.58\tau_{MODIS} + 0.17$. The large negative differences are located in the South Xinjiang Basin and East China such as the Beijing-Tianjin-Hebei region and the Yangtze River Delta, where the MODIS AODs are higher than in other areas. The reason for this difference may be that in these areas the land cover types, namely, desert in Xinjiang and urban in East China, restrict the accuracy of LABITS, for similar reasons as in SAH and IND as discussed in Section 3.1. In addition, the lack of data filtering and quality control in the operational application of the LABITS algorithm may decrease the quality, i.e. in the AVHRR AOD monthly calculation we averaged all valid retrievals, including some with poor quality. After averaging, the clearly high AODs are removed. This phenomenon is also apparent in other regions where the differences with the MODIS AOD values are mostly positive and greater than 0.15. In these regions, the unreliable high retrievals, which may be due to cloud contamination, calibration accuracy, observation geometry, or retrieval algorithm, are not removed and are employed for averaging.

For validation of LABITS AOD over China the results are compared with AERONET data. A scatterplot of LABITS-AOD vs. AERONET-AOD is presented in Fig. 18. In this plot, $R^2 = 0.79$, RMSE = 0.13, and the regression equation is $\tau_{AVHRR} = 0.92\tau_{AERONET} + 0.09$. AERONET AOD values are generally used as ground truth with a much higher accuracy than satellite data. Therefore we evaluate the LABITS AVHRR uncertainty based on the comparison with AERONET data as $\Delta\tau = \pm0.05 \pm 0.30\tau$.

Time series daily AVHRR and MODIS AOD measurements over some selected AERONET sites are compared with daily-averaged AERONET AOD values in Fig. 19. AERONET AOD was interpolated to the wavelength same as AVHRR AOD using Eq. (18). The four sites, Xianghe (39.8°N, 117.0°E), Shouxian (32.6°N, 116.8°E), Noto (37.3°N, 137.1°E), and Ussuriysk (43.7°N, 132.2°E), are selected because for these sites there are sufficient data from AVHRR, MODIS and ground measurements in the investigated month. At other sites less data were available, e.g. because of the occurrence of clouds which prevented AVHRR

aerosol retrieval. Note that in the LABITS algorithm, if one pixel in the 2×2-pixel window is cloudy during one overpass in the four-observation period, no retrieval is made.

At each of the four sites shown in Fig. 19, the AVHRR AODs are generally less than 1.0. Although the AODs from the AERONET site are daily averaged and the measurement times are not matched with the satellite observations, the satellite and AERONET data trace quite well. However, on some days, e.g., 08/28/2008 in Xianghe and 08/03/2008 in Shouxian, the AVHRR AODs are much lower than the MODIS and AERONET measurements, whereas on others, e.g., 08/13/2008 in Noto and 08/27/2008 in Ussuriysk, the AVHRR AODs are higher than MODIS and AERONET AODs. This finding indicates that the LABITS algorithm is not stable in certain cases. Differences may be caused by several factors: (1) the accuracy of the RT model and BRF model, (2) the representation of aerosol types, (3) land cover types, (4) cloud contamination, and (5) calibration uncertainty, which we have discussed above. In general, for many days over the sites, the AVHRR AODs are similar to other AOD products such as MODIS and AERONET.

From the AOD results from the NOAA-18 AVHRR data over China, the algorithm is applicable and the daily AOD retrieval has a good accuracy in many cases. For the monthly averaged AOD, data filtering and quality control are needed to obtain more reliable aerosol products.

4. Discussion and conclusion

In this paper, we present an algorithm, LABITS, for AOD and BRF retrieval over land, and apply it to NOAA AVHRR data for the first time, over different time periods and regions. First, the algorithm can retrieve several parameters of the earth-atmosphere system, including AOD, BRF and albedo. Second, the algorithm is validated for many land cover types, such as vegetation and desert. Third, because there is only one channel employed in the algorithm, it is portable and suitable for a satellite sensor with a single visible channel, such as AVHRR. The algorithm has the potential to retrieve long-term global AOD over land from NOAA AVHRR data from as far back as the 1980s and is useful for the study of aerosol climatology and global climate change. Moreover, the resolution of the AOD retrieved by the algorithm is $0.1° \times 0.1°$ (approximately 10 km × 10 km), which is higher than that retrieved by some other similar algorithms because the window size is
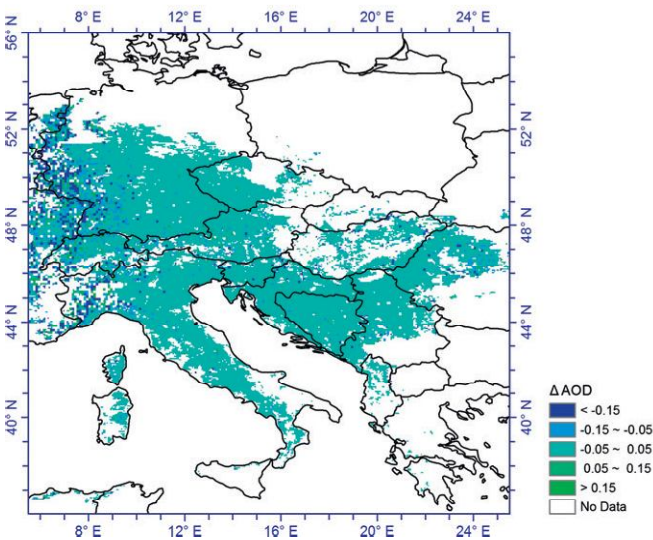
(a) Difference map of AOD from NOAA-15 and NOAA-16 satellites over EUR on 08/15/2001
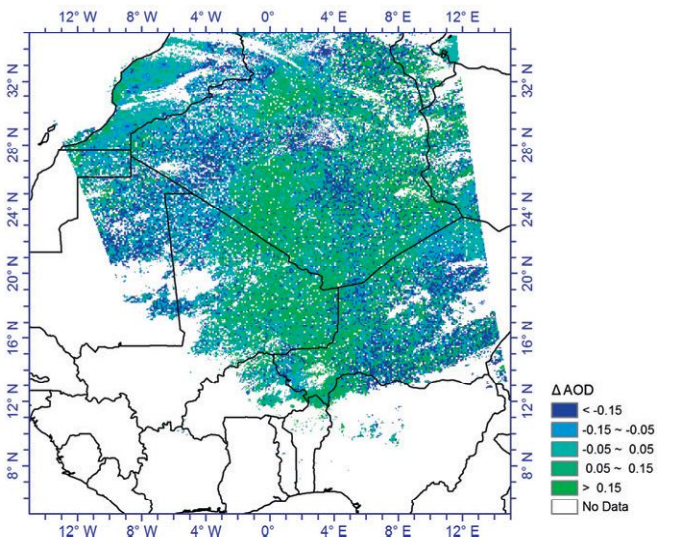
(a) Difference map of AOD from NOAA-16 and NOAA-18 satellites over SAH on 04/29/2006

Fig. 7. Difference maps for AODs obtained from different satellite platforms on the same day. (a) Difference map of AOD from NOAA-15 and NOAA-16 satellites over EUR on 08/15/2001; (b) Difference map of AOD from NOAA-16 and NOAA-18 satellites over SAH on 04/29/2006.

2 pixels × 2 pixels, within which we assume that the aerosol characteristics are constant. In contrast, in other similar algorithms, e.g. that proposed by Hauser et al. (2005b) and Lyapustin et al. (2011a,b), the window size is usually 25 pixels × 25 pixels, corresponding to a resolution of 25 km × 25 km.

The main disadvantage of the use of the LABITS algorithm is the requirement of strict cloud detection. In the LABITS algorithm, four cloud-free observations are required. If one observation is cloud- or snow/ice-contaminated, no retrieval can be made. A lack of precision for coarse-mode dominated aerosol is also found in this study, calling
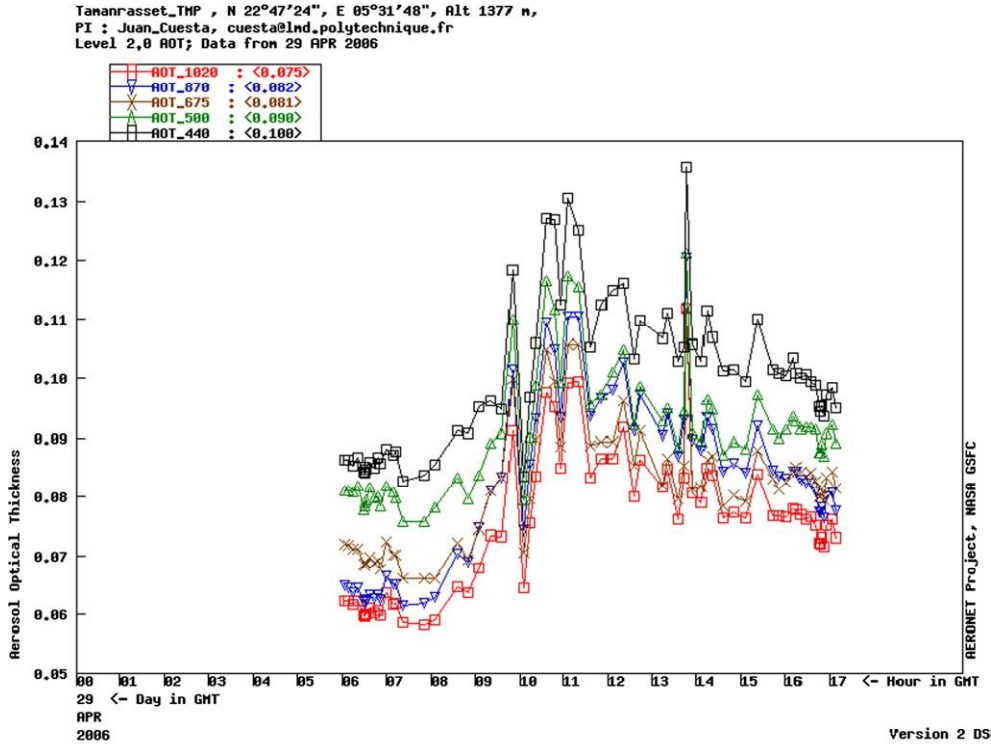
(a) Diurnal variation of AOD aerosol size distribution
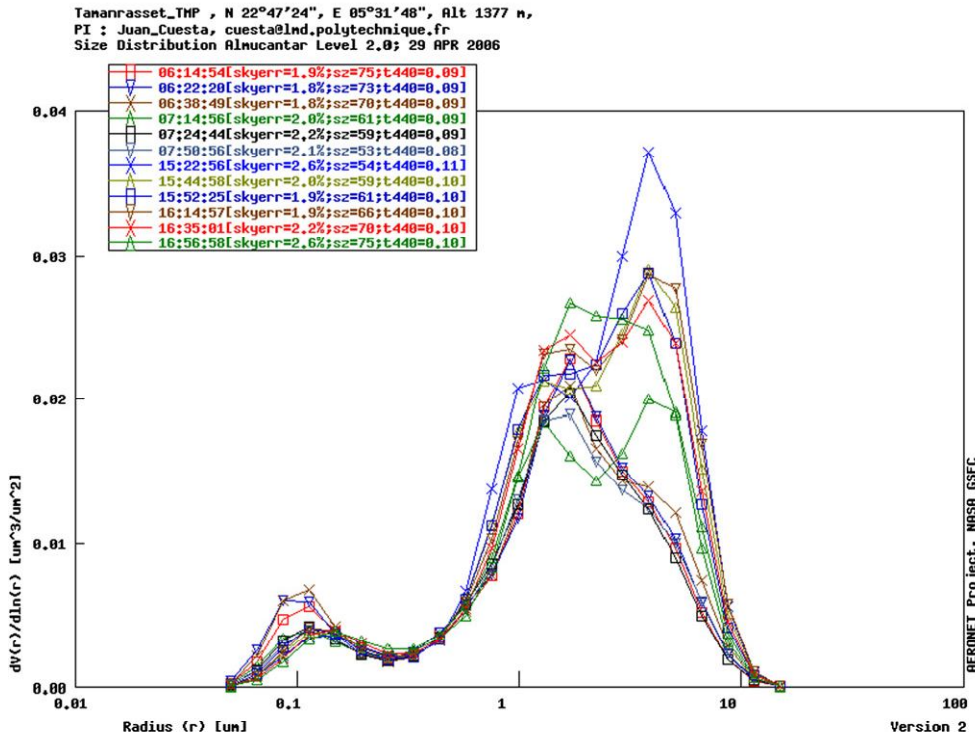
(b) Diurnal variation of aerosol size distribution

Fig. 8. Diurnal variation of AOD and size distribution at Tamanrasset_TMP site on 04/29/2006. (a) Diurnal variation of AOD and (b) diurnal variation of aerosol size distribution.

for a modification of the modeling of the aerosol scattering in the future. In addition, retrieving long-term AOD over land from NOAA AVHRR data entails some inevitable problems, such as the estimation of the historical aerosol properties, cross-calibration for historical NOAA AVHRR data and massive data processing. The follow-up study will include the validation of the algorithm using more data, improving the RT model precision and the algorithm flexibility, analyzing the uncertainties for different aerosol and land cover types, and studying the data quality control and filtering techniques for monthly aerosol products.

Acknowledgments
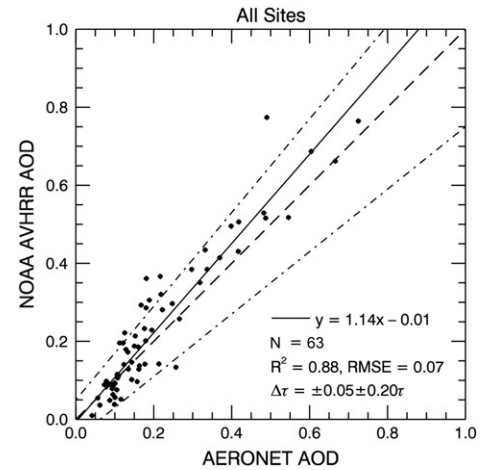
Fig. 10. NOAA-retrieved AOD comparison with AERONET data at all sites.
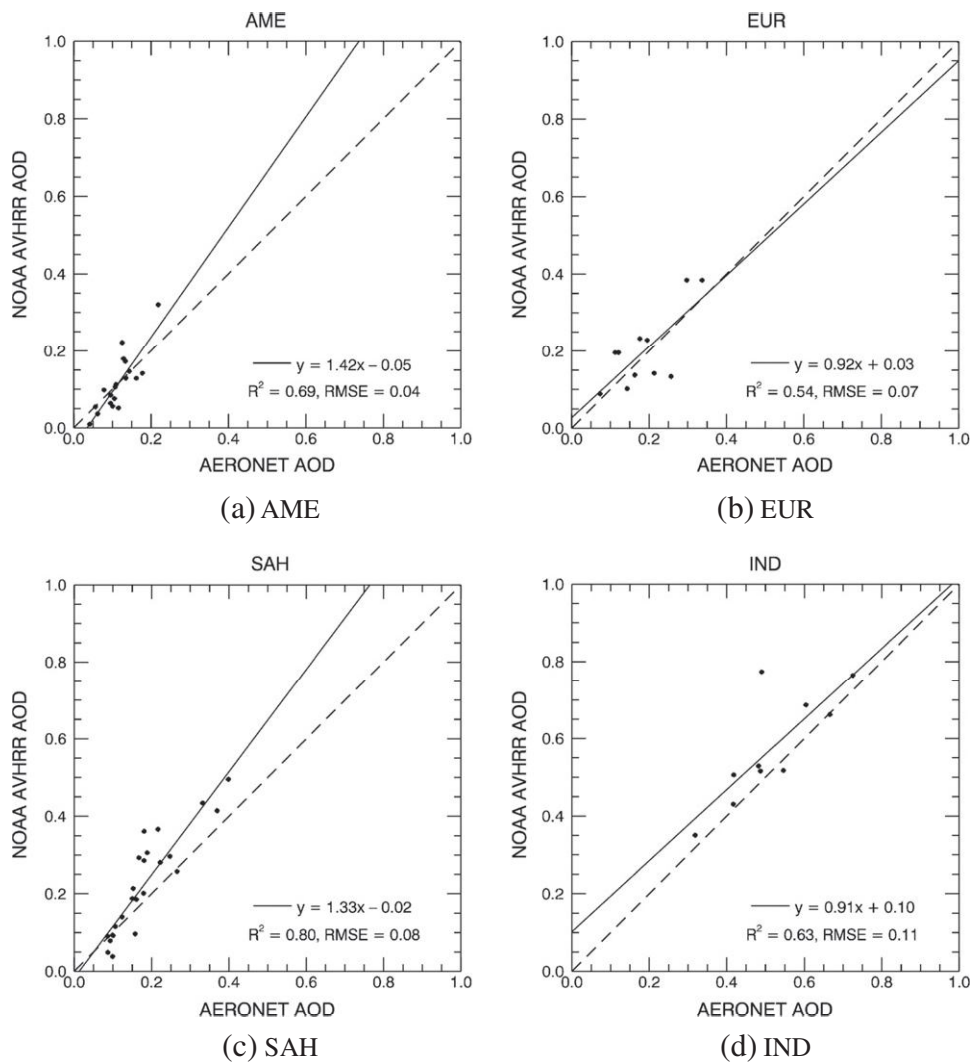

(a) AME

(b) EUR

(c) SAH

(d) IND

Fig. 9. NOAA-retrieved AOD comparison with AERONET data for the ROIs. (a) AME; (b) EUR; (c) SAH and (d) IND.

Appendix A. Multiple-scattered radiance estimation by two-stream approximation

The general two-stream approximation proposed by Meador and Weaver (1980) can be expressed as
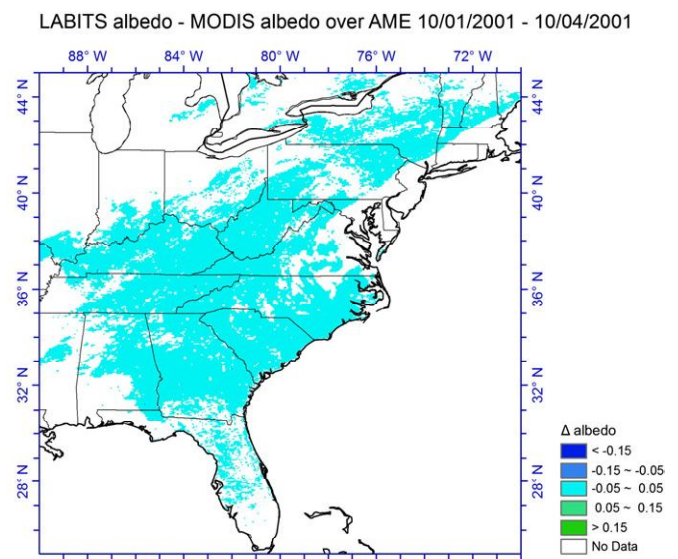
$$\begin{cases} \dfrac{dI^+(\tau)}{d\tau} = \gamma_1 I^+(\tau) - \gamma_2 I^-(\tau) - \pi F'_0 \omega_a \gamma_3 \exp\left(-\dfrac{\tau}{|\mu_s|}\right) \\ \dfrac{dI^-(\tau)}{d\tau} = \gamma_2 I^+(\tau) - \gamma_1 I^-(\tau) + \pi F'_0 \omega_a \gamma_4 \exp\left(-\dfrac{\tau}{|\mu_s|}\right) \end{cases}. \qquad \text{(A1)}$$

For the hybrid modified Eddington-delta approximation, the coefficients are (Meador & Weaver, 1980)
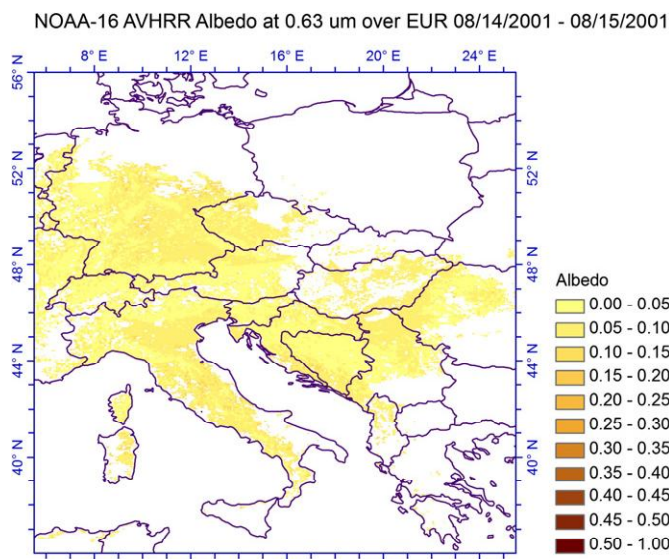
$$\begin{cases} \gamma_1 = \dfrac{7 - 3g_a^2 - \omega_a(4 + 3g_a) + \omega_a g_a^2(4\beta_a + 3g_a)}{4[1 - g_a^2(1 - |\mu_s|)]} \\ \gamma_2 = \dfrac{g_a^2 - 1 + \omega_a(4 - 3g_a) + \omega_a g_a^2(4\beta_a + 3g_a - 4)}{4[1 - g_a^2(1 - |\mu_s|)]} \\ \gamma_3 = \beta_a \\ \gamma_4 = 1 - \beta_a \end{cases} \qquad \text{(A2)}$$
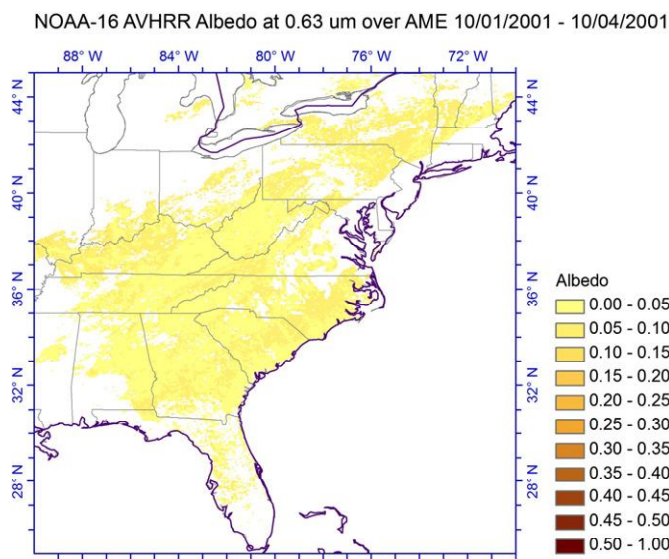
Fig. 11. Albedo maps retrieved with the LABITS algorithm and the differences between LABITS and MODIS retrievals over the ROIs. (a1) LABITS albedo over AME; (a2) LABITS albedo–MODIS albedo over AME; (b1) LABITS albedo over EUR; (b2) LABITS albedo–MODIS albedo over EUR; (c1) LABITS albedo over SAH; (c2) LABITS albedo–MODIS albedo over SAH; (d1) LABITS albedo over IND; (d2) LABITS albedo–MODIS albedo over IND.
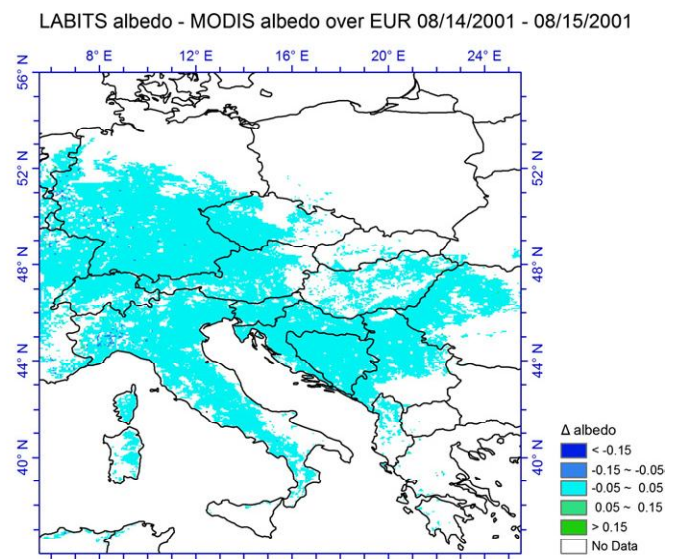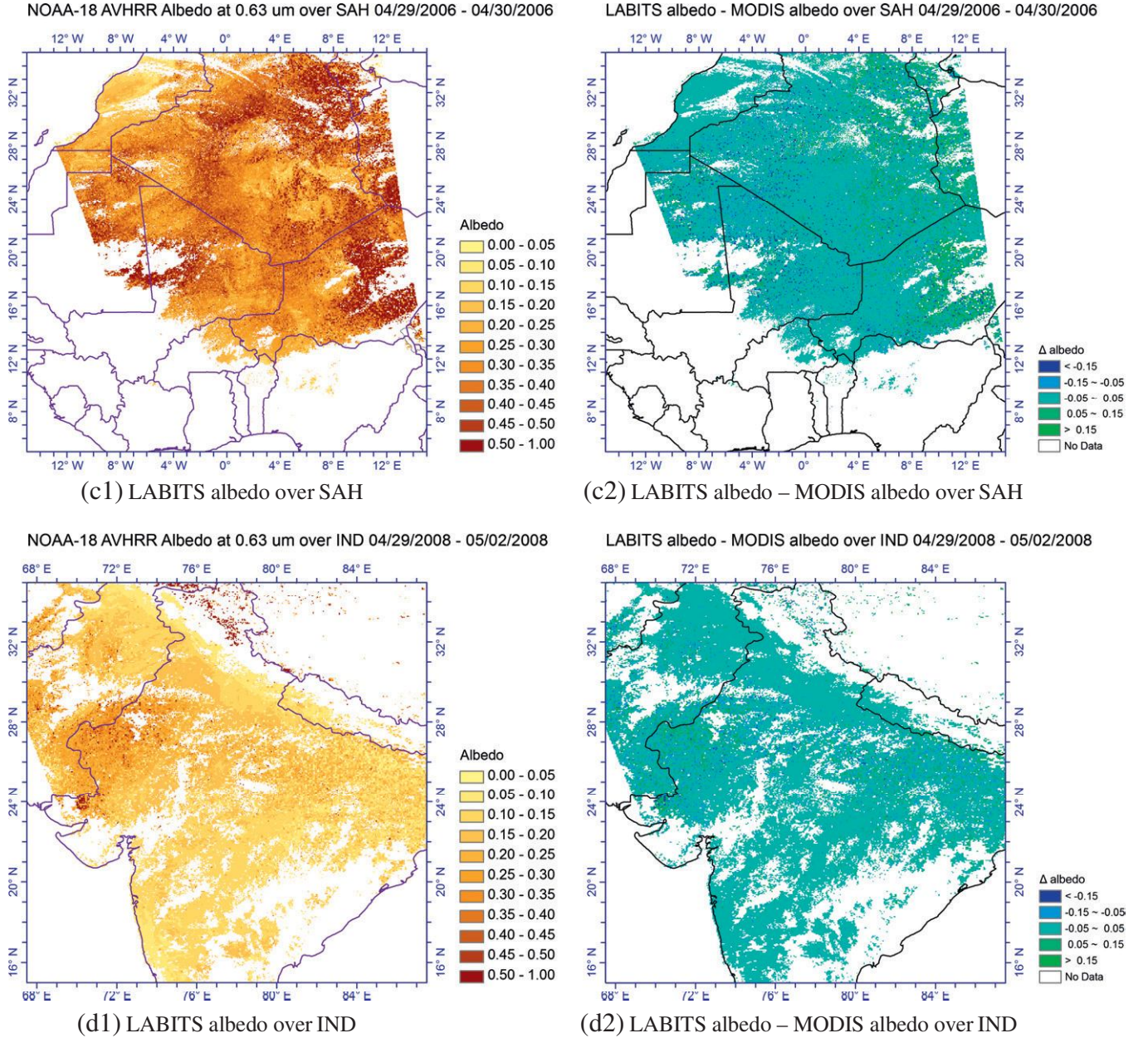
(c1) LABITS albedo over SAH

(c2) LABITS albedo – MODIS albedo over SAH

(d1) LABITS albedo over IND

(d2) LABITS albedo – MODIS albedo over IND

Fig. 11 (*continued*).

and the backscattering ratio β_a can be calculated by (Liou, 2002)

$$\beta_a = \frac{1}{2}\int_{-1}^{1} P_a(\Theta)\frac{1-\cos(\Theta)}{2}\,\mathrm{d}\cos(\Theta) = \frac{1-g_a}{2}. \tag{A3}$$

From Eq. (A1), we obtain the general solutions as

$$\begin{cases} I^+(\tau) = X_1\exp(\eta\tau) + X_2\exp(-\eta\tau) + X_3\exp\left(-\tau\left|\mu_s^{-1}\right|\right) \\ I^-(\tau) = \dfrac{\gamma_1-\eta}{\gamma_2}X_1\exp(\eta\tau) + \dfrac{\gamma_1+\eta}{\gamma_2}X_2\exp(-\eta\tau) \\ \qquad + \dfrac{1}{\gamma_2}\left[\left(\gamma_1+\left|\mu_s^{-1}\right|\right)X_3 - \pi F'_0\omega_a\gamma_3\right]\exp\left(-\tau\left|\mu_s^{-1}\right|\right) \end{cases} \tag{A4}$$

where

$$\eta = \sqrt{\gamma_1^2-\gamma_2^2} \tag{A5}$$

$$X_3 = -\left(\gamma_1\gamma_3 + \gamma_2\gamma_4 - \gamma_3\left|\mu_s^{-1}\right|\right)\frac{\mu_s^2\pi F'_0\omega_a}{1-\mu_s^2\eta^2} \tag{A6}$$

and X_1 and X_2 are determined from the boundary conditions. Because the reflectance of direct radiance is quantified by the direct radiance and the Ross–Li BRF model, we only account for diffuse radiance. Obviously, there is no diffuse radiance at the TOA ($\tau = 0$), and at the bottom of the atmosphere (BOA) ($\tau = \tau_a$), the reflectance can be expressed as the white-sky albedo, α. Therefore, we have

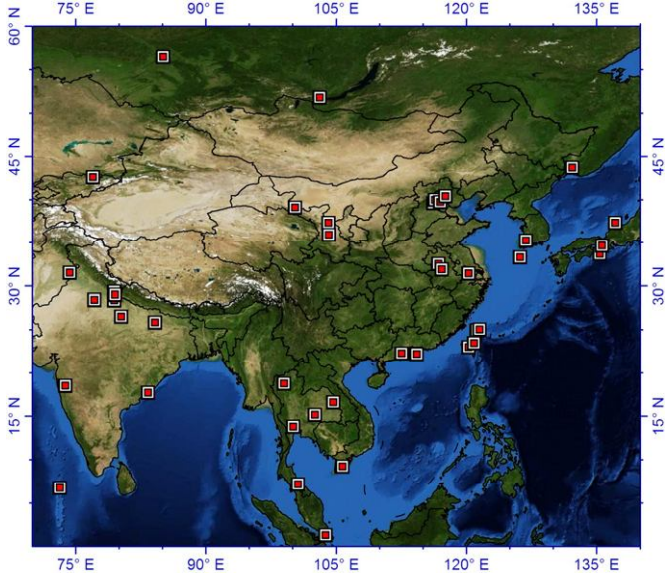$$\begin{cases} I^-(0) = 0 \\ I^+(\tau_a) = \alpha I^-(\tau_a) \end{cases}. \tag{A7}$$

Fig. 12. Map of the study and locations of AERONET sites over China.

Thus, we obtain the expressions of X_1 and X_2 in Eq. (A4) as

$$
\begin{cases}
X_1 = \dfrac{u(\gamma_1 + \eta)\exp\left(-\tau_a \left|\mu_s^{-1}\right|\right) - v[\gamma_2 - (\gamma_1 + \eta)\alpha]\exp(-\eta\tau_a)}{(\gamma_1 - \eta)[\gamma_2 - (\gamma_1 + \eta)\alpha]\exp(-\eta\tau_a) - (\gamma_1 + \eta)[\gamma_2 - (\gamma_1 - \eta)\alpha]\exp(\eta\tau_a)} \\
X_2 = \dfrac{-u(\gamma_1 - \eta)\exp\left(-\tau_a \left|\mu_s^{-1}\right|\right) + v[\gamma_2 - (\gamma_1 - \eta)\alpha]\exp(\eta\tau_a)}{(\gamma_1 - \eta)[\gamma_2 - (\gamma_1 + \eta)\alpha]\exp(-\eta\tau_a) - (\gamma_1 + \eta)[\gamma_2 - (\gamma_1 - \eta)\alpha]\exp(\eta\tau_a)}
\end{cases}
$$

(A8)

where

$$
\begin{aligned}
u &= \left[\gamma_2 - \alpha\left(\gamma_1 + \left|\mu_s^{-1}\right|\right)\right]X_3 + \pi F'_0 \alpha \omega_a \gamma_3 \\
v &= \left(\gamma_1 + \left|\mu_s^{-1}\right|\right)X_3 - \pi F'_0 \omega_a \gamma_3.
\end{aligned}
$$

(A9)

We define the total diffuse upward flux calculated by Eqs. (A4) through (A8) as $I_T^+(\tau)$. Notice that it includes the single-scattering

flux $I_1^+(\tau)$ and the multiple-scattering flux $I_M^+(\tau)$. Therefore, we can obtain $I_M^+(\tau)$ by

$$
I_M^+(\tau) = I_T^+(\tau) - I_1^+(\tau).
$$

(A10)

To calculate $I_1^+(\tau)$, the surface albedo α in Eq. (A7) is set to zero, and the two-stream coefficients, γ_1 and γ_2, should be modified as γ'_1 and γ'_2 (Liang & Strahler, 1993, 1994):

$$
\begin{cases}
\gamma'_1 = \dfrac{7 - 3g_a^2}{4\left[1 - g_a^2(1 - |\mu_s|)\right]} \\
\gamma'_2 = \dfrac{g_a^2 - 1}{4\left[1 - g_a^2(1 - |\mu_s|)\right]}
\end{cases}.
$$

(A11)

In the corresponding solution, X_3 is the same as in Eq. (A6) and X_1 and X_2 are modified as

$$
\begin{cases}
X'_1 = \dfrac{\left(\gamma'_1 + \eta\right)X_3 \exp\left(-\tau_a\left|\mu_s^{-1}\right|\right) - \left[\left(\gamma'_1 + \left|\mu_s^{-1}\right|\right)X_3 - \pi F'_0 \omega_a \gamma_3\right]\exp(-\eta\tau_a)}{(\gamma'_1 - \eta)\exp(-\eta\tau_a) - (\gamma'_1 + \eta)\exp(\eta\tau_a)} \\
X'_2 = \dfrac{-\left(\gamma'_1 - \eta\right)X_3 \exp\left(-\tau_a\left|\mu_s^{-1}\right|\right) + \left[\left(\gamma'_1 + \left|\mu_s^{-1}\right|\right)X_3 - \pi F'_0 \omega_a \gamma_3\right]\exp(\eta\tau_a)}{(\gamma'_1 - \eta)\exp(-\eta\tau_a) - (\gamma'_1 + \eta)\exp(\eta\tau_a)}
\end{cases}.
$$

(A12)

After obtaining the multiple-scattering flux at the TOA, we have to convert it to the radiance, which is observed by satellite sensors. By employing the hybrid Eddington-delta algorithm, we have the approximation of the upward radiance integrated by the azimuth angle (Meador & Weaver, 1980):

$$
I(\tau, \mu_v) = \frac{1}{1 - g_a^2(1 - |\mu_s|)}\left\{\left(1 - g_a^2\right)\left[(1 + 1.5\mu_v)I^+(\tau) + (1 - 1.5\mu_v)I^-(\tau)\right] + g_a^2\delta(\mu_v + \mu_s)I^+(\tau)\right\}
$$

(A13)

and the radiance is

$$
I(\tau, \Omega_v) = \frac{I(\tau, \mu_v)}{2\pi}.
$$

(A14)
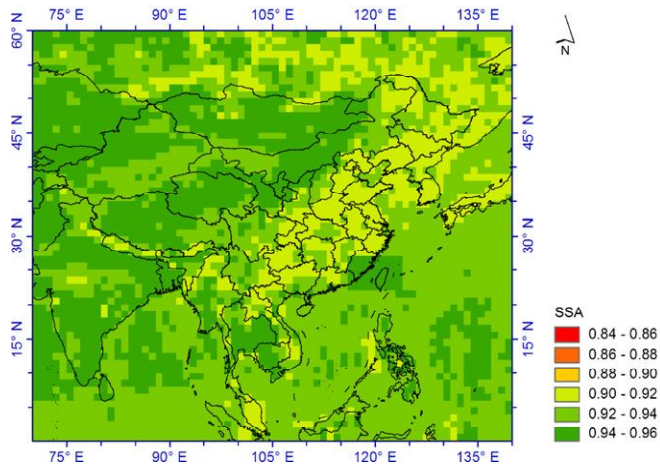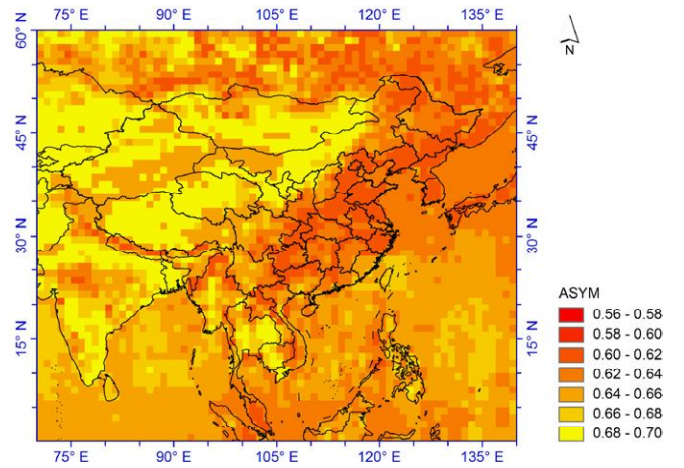
Fig. 13. Maps of aerosol SSA and ASYM at 0.63 μm over China in August 2008. (a) SSA and (b) ASYM.

NOAA-18 AVHRR AOD at 0.63 um over China on 08/04/2008

(a) AOD from NOAA AVHRR data

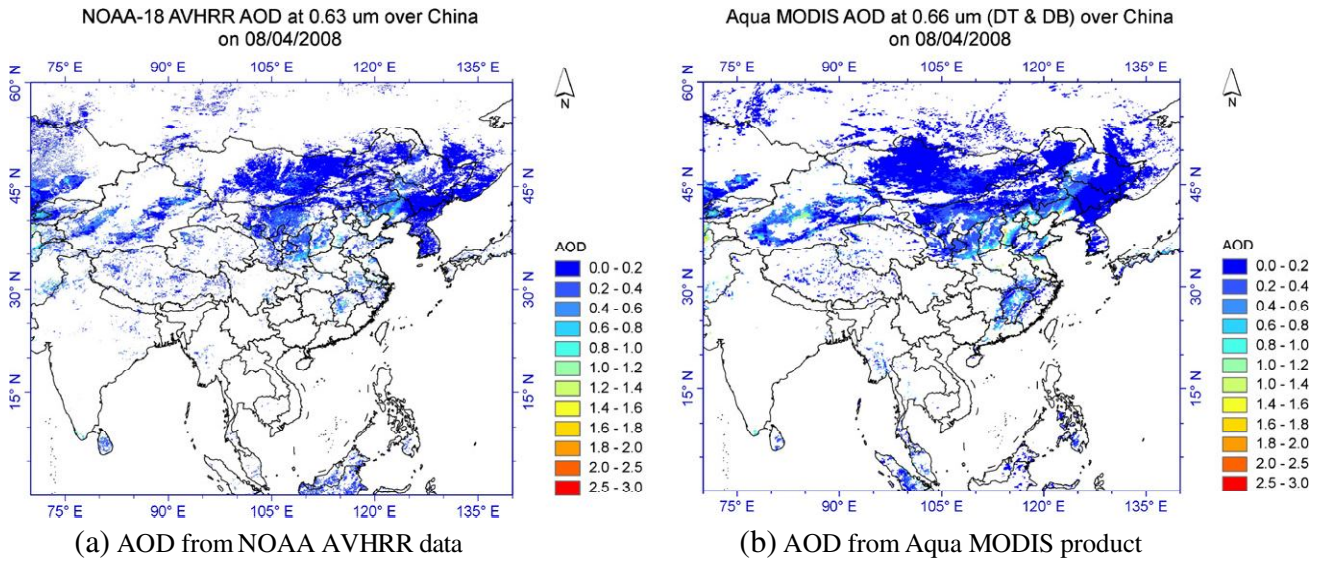## Aqua MODIS AOD at 0.66 um (DT & DB) over China on 08/04/2008

(b) AOD from Aqua MODIS product

Fig. 14. AOD from AVHRR and MODIS on 08/04/2008 (Resolution: 0.1°×0.1°). (a) AODs from NOAA AVHRR data and (b) AODs from Aqua MODIS product.

NOAA-18 AVHRR AOD at 0.63 um over China Monthly Average of 08/2008

(a) AOD from NOAA AVHRR data

MYD08_M3 AOD at 0.66 um (DT & DB) over China Monthly Average of 08/2008

(b) AOD from Aqua MODIS product
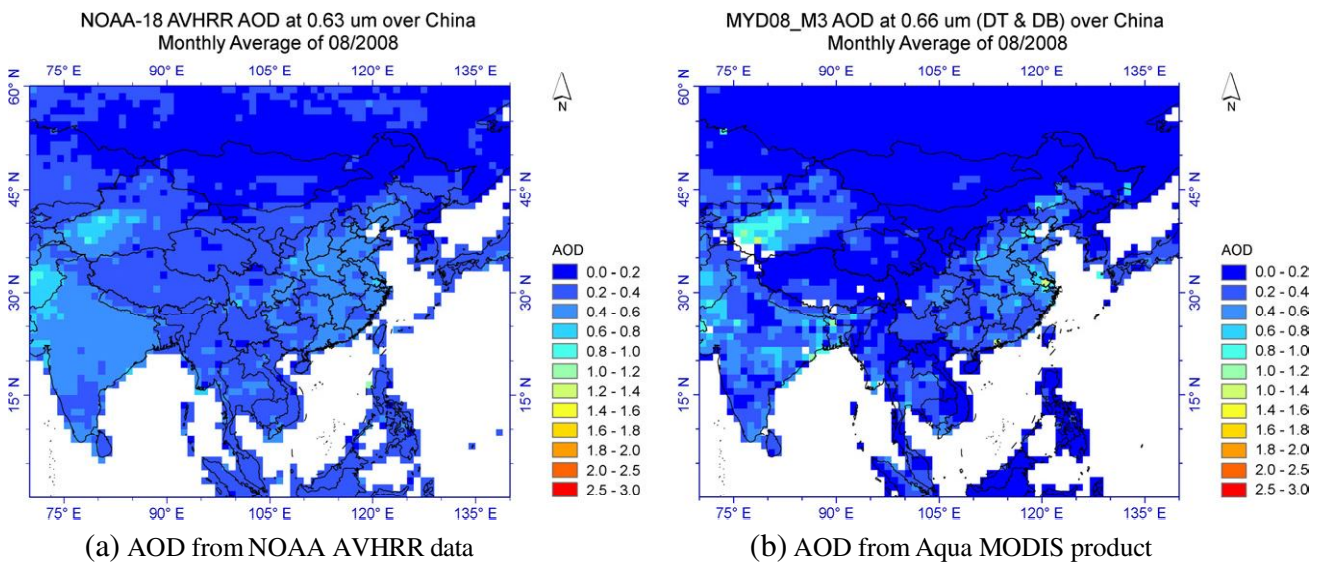
Fig. 15. Monthly AOD from AVHRR and MODIS of August 2008 (Resolution: 1°×1°). (a) AODs from NOAA AVHRR data and (b) AODs from Aqua MODIS product.

LABITS AOD (NOAA-18) - MODIS AOD (MYD04) over China on 08/04/2008

(a) Difference map for 08/04/2008

N=34744
Y=0.93x+0.02
R²=0.75; RMS=0.11

(b) Scatter diagram for 08/04/2008

Fig. 16. Difference map between AVHRR and MODIS AODs and scatter diagram for 08/04/2008. (a) Difference map for 08/04/2008 and (b) scatter diagram for 08/04/2008.

(a) Difference map for August 2008

(b) Scatter diagram for August 2008.

Fig. 17. Difference map between AVHRR and MODIS AODs and scatter diagram for August 2008. (a) Difference map for August 2008 and (b) Scatter diagram for August 2008.
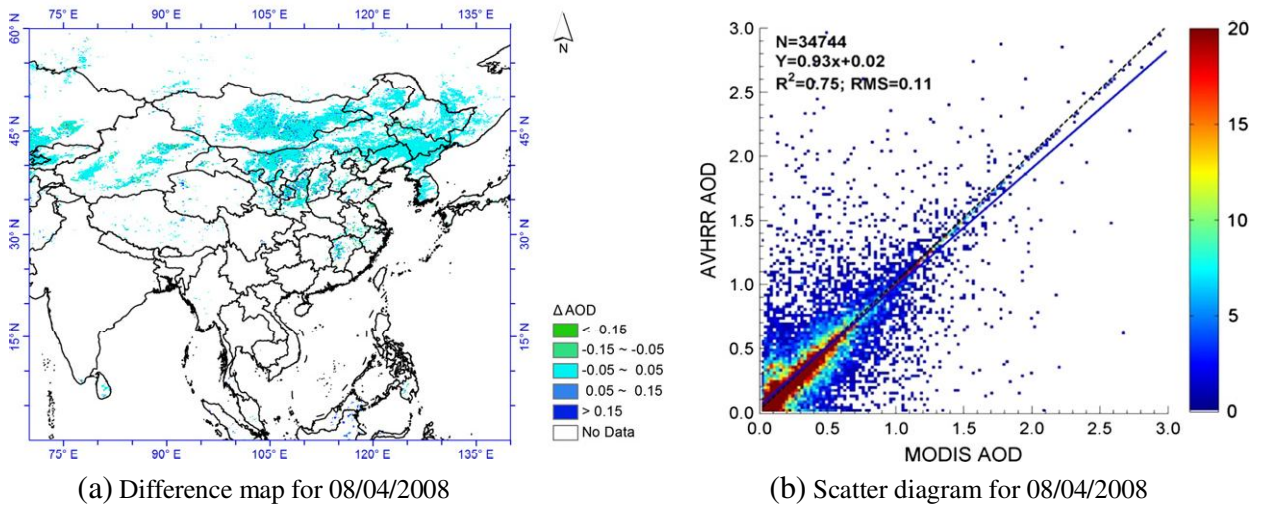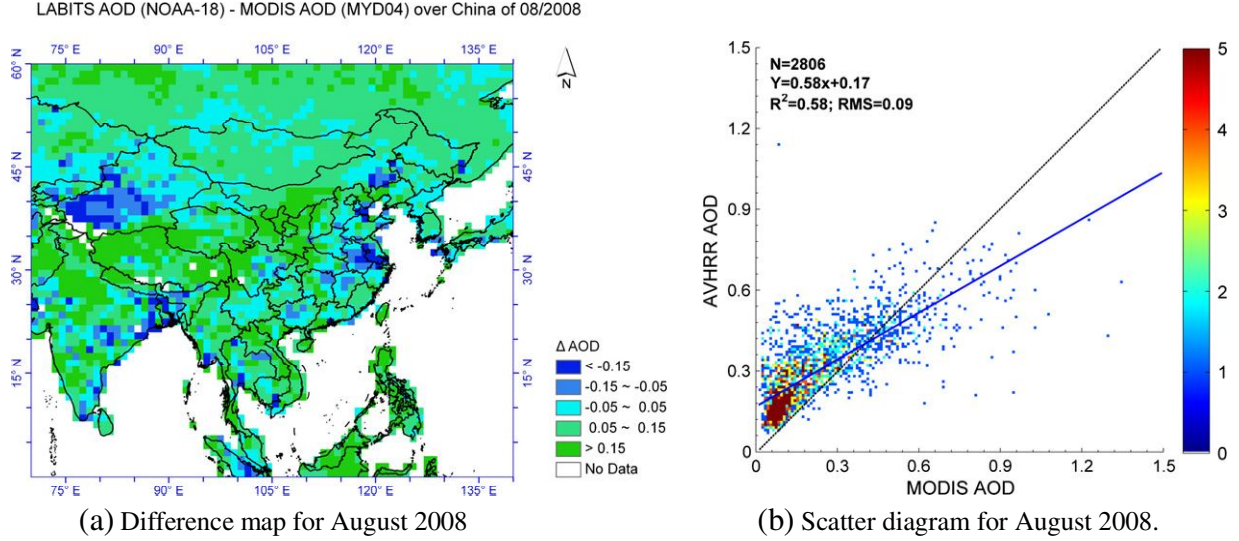
Therefore, the multiple-scattering radiance at the TOA is written as

$$
\begin{aligned}
I_M(0, \Omega_v) &= \frac{I_T(0, \mu_v) - I_1(0, \mu_v)}{2\pi} \\
&= \frac{\left(1 - g_a^2\right)(1 + 1.5\mu_v)\left[I_T^+(0) - I_1^+(0)\right] + g_a^2 \delta(\mu_v + \mu_s)\left[I_T^+(0) - I_1^+(0)\right]}{2\pi\left[1 - g_a^2(1 - |\mu_s|)\right]}.
\end{aligned}
$$

(A15)

It is possible to incorporate a δ-function adjustment to account for the forward scattering peak in the context of the two-stream approximation (Joseph & Wiscombe, 1976; Liang & Strahler, 1994). If a fraction of the scattering energy, f, which is most frequently defined as $f = g_{ae}^2$, is considered to be in the forward peak, the above formulas can still be used as long as the following transformations are made in the coefficients:

$$
\begin{aligned}
\tau'_{ae} &= (1 - \omega_{ae}f)\tau_{ae} \\
\omega'_{ae} &= \frac{(1 - f)\omega_{ae}}{1 - \omega_{ae}f} \\
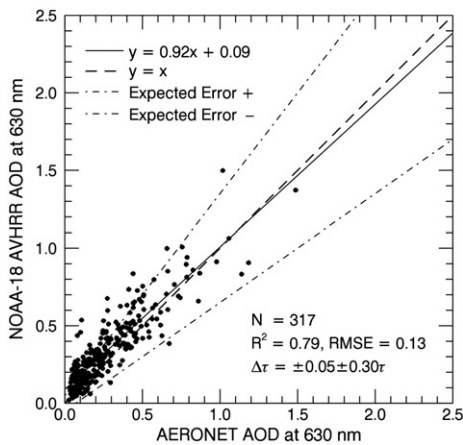g'_{ae} &= \frac{g_{ae} - f}{1 - f}.
\end{aligned}
$$

(A16)

Fig. 18. AOD Comparison with AERONET AOD data over China in August 2008.

Appendix B. Details of the Ross–Li BRF Model

The Ross–Li BRF model is written as (Wanner et al., 1995)

$$
\rho(\theta_s, \theta_v, \varphi_s - \varphi_v) = f_{iso} K_{iso} + f_{vol} K_{vol} + f_{geo} K_{geo}.
$$

(B1)

The expressions of each kernel are

$$
\begin{aligned}
K_{iso} &= 1 \\
K_{vol} &= \frac{(\pi/2 - \xi)\cos(\xi) + \sin(\xi)}{\cos(\theta_s) + \cos(\theta_v)} - \frac{\pi}{4} \\
K_{geo} &= O(\theta_s, \theta_v, \varphi_s - \varphi_v) - \sec\left(\theta'_s\right) - \sec\left(\theta'_v\right) + \frac{1}{2}\left[1 + \cos\left(\xi'\right)\right]\sec\left(\theta'_s\right)\sec\left(\theta'_v\right)
\end{aligned}
$$

(B2)

where

$$
\begin{aligned}
\cos(\xi) &= \cos(\theta_s)\cos(\theta_v) + \sin(\theta_s)\sin(\theta_v)\cos(\varphi_s - \varphi_v) \\
O &= \frac{1}{\pi}[t - \sin(t)\cos(t)]\left[\sec\left(\theta'_s\right) + \sec\left(\theta'_v\right)\right] \\
\cos(t) &= \frac{h}{b}\frac{\sqrt{D^2 + \left[\tan(\theta'_s)\tan(\theta'_v)\sin(\varphi_s - \varphi_v)\right]^2}}{\sec\left(\theta'_s\right) + \sec\left(\theta'\right)} \\
D &= \sqrt{\tan^2\left(\theta'_s\right) + \tan^2\left(\theta'_v\right) - 2\tan\left(\theta'_s\right)\tan\left(\theta'_v\right)\cos(\varphi_s - \varphi_v)} \\
\cos\left(\xi'\right) &= \cos\left(\theta'_s\right)\cos\left(\theta'_v\right) + \sin\left(\theta'_s\right)\sin\left(\theta'_v\right)\cos(\varphi_s - \varphi_v) \\
\theta'_s &= \tan^{-1}\left[\frac{b}{r}\tan(\theta_s)\right] \\
\theta'_v &= \tan^{-1}\left[\frac{b}{r}\tan(\theta_v)\right].
\end{aligned}
$$

(B3)

Here, O is the overlap area between the view and the solar shadows. The term $\cos(t)$ should be constrained to the range $[-1, 1]$, as values outside of this range imply that there is no overlap and should be disregarded. Note that the dimensionless crown relative height and shape parameters h/b and b/r are within the kernel and should therefore be pre-selected (Wanner et al., 1995). For the MODIS processing and the AVHRR examples given in this paper, $h = b = 2$ and $b = r = 1$, meaning that the spherical crowns are separated from the ground by half their diameter. Generally, the shape of the crowns affects the BRDF more than that by their relative height (Strahler & Muller, 1999).
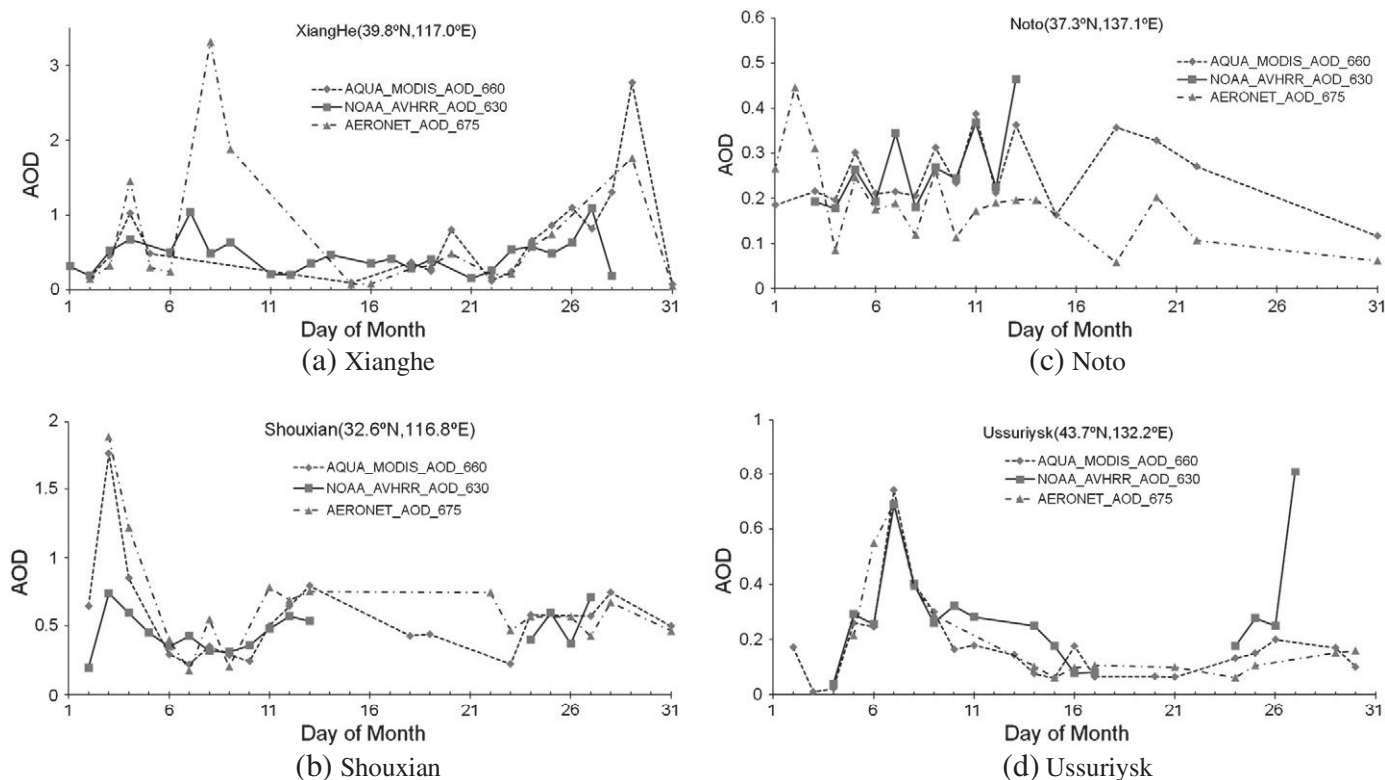
Fig. 19. Time series AOD from AVHRR, MODIS and AERONET measurements over the four AERONET sites. (a) Xianghe; (b) Shouxian; (c) Noto and (d) Ussuriysk.

References

Asakuma, K., Minomura, M., Otsutsumi, S., Kuze, H., & Takeuchi, N. (2002). Estimation of aerosol optical thickness over land in Chiba area from AVHRR data. In J. P. Burrows, & N. Takeuchi (Eds.), *Remote sensing of trace constituents in the lower stratosphere, troposphere and the earth's surface: Global observations, air pollution and the atmospheric correction* (pp. 1747–1752). Oxford: Pergamon.

Bird, R. E., & Riordan, C. (1986). Simple solar spectral model for direct and diffuse irradiance on horizontal and tilted planes at the Earth's surface for cloudless atmospheres. *Journal of Climate and Applied Meteorology, 25*, 87–97.

Carrer, D., Roujean, J. -L., Hautecoeur, O., & Elias, T. (2010). Daily estimates of aerosol optical thickness over land surface based on a directional and temporal analysis of SEVIRI MSG visible observations. *Journal of Geophysical Research-Atmospheres, 115*, D10208. http://dx.doi.org/10.1029/2009JD012272.

Deuzé, J. L., Bréon, F. M., Devaux, C., Goloub, P., Herman, M., Lafrance, B., et al. (2001). Remote sensing of aerosols over land surfaces from POLDER-ADEOS-1 polarized measurements. *Journal of Geophysical Research, 106*, 4913–4926.

Diner, D. J., Beckert, J. C., Reilly, T. H., Bruegge, C. J., Conel, J. E., Kahn, R. A., et al. (1998). Multi-angle imaging spectroradiometer (MISR) instrument description and experiment overview. *IEEE Transactions on Geoscience and Remote Sensing, 36*, 1072–1087.

Diner, D. J., Martonchik, J. V., Kahn, R. A., Pinty, B., Gobron, N., Nelson, D. L., et al. (2005). Using angular and spectral shape similarity constraints to improve MISR aerosol and surface retrievals over land. *Remote Sensing of Environment, 94*, 155–171.

Dubovik, O., & King, M. D. (2000). A flexible inversion algorithm for retrieval of aerosol optical properties from Sun and sky radiance measurements. *Journal of Geographical Research, 105*, 20673–20696.

Dubovik, O., Smirnov, A., Holben, B. N., King, M. D., Kaufman, Y. J., Eck, T. F., et al. (2000). Accuracy assessments of aerosol optical properties retrieved from Aerosol Robotic Network (AERONET) Sun and sky radiance measurements. *Journal of Geophysical Research-Atmospheres, 105*, 9791–9806.

Eck, T. F., Holben, B. N., Reid, J. S., Dubovik, O., Smirnov, A., O'Neill, N. T., et al. (1999). Wavelength dependence of the optical depth of biomass burning, urban, and desert dust aerosols. *Journal of Geophysical Research-Atmospheres, 104*, 31333–31349.

Emili, E., Lyapustin, A., Wang, Y., Popp, C., Korkin, S., Zebisch, M., et al. (2011). High spatial resolution aerosol retrieval with MAIAC: Application to mountain regions. *Journal of Geophysical Research, 116*, D23211. http://dx.doi.org/10.1029/2011JD016297.

Govaerts, Y. M., Wagner, S., Lattanzio, A., & Watts, P. (2010). Joint retrieval of surface reflectance and aerosol optical depth from MSG/SEVIRI observations with an optimal estimation approach: 1. Theory. *Journal of Geophysical Research-Atmospheres, 115*, D02203. http://dx.doi.org/10.1029/2009JD011779.

Hapke, B. (1981). Bidirectional reflectance spectroscopy: 1. Theory. *Journal of Geophysical Research, 86*, 3039–3054.

Hauser, A., Oesch, D., & Foppa, N. (2005). Aerosol optical depth over land: Comparing AERONET, AVHRR and MODIS. *Geophysical Research Letters, 32*, L17816. http://dx.doi.org/10.1029/2005GL023579.

Hauser, A., Oesch, D., Foppa, N., & Wunderle, S. (2005). NOAA AVHRR derived aerosol optical depth over land. *Journal of Geophysical Research-Atmospheres, 110*, D08204. http://dx.doi.org/10.1029/2004JD005439.

Henyey, L. G., & Greenstein, J. L. (1941). Diffuse radiation in the galaxy. *The Astrophysical Journal, 93*, 70–83.

Holben, B., Vermote, E., Kaufman, Y. J., Tanre, D., & Kalb, V. (1992). Aerosol retrieval over land from AVHRR data — Application for atmospheric correction. *IEEE Transactions on Geoscience and Remote Sensing, 30*, 212–222.

Hsu, N. C., Tsay, S. -C., King, M. D., & Herman, J. R. (2004). Aerosol properties over bright-reflecting source regions. *IEEE Transactions on Geoscience and Remote Sensing, 42*, 557–569.

Hsu, N. C., Tsay, S. -C., King, M. D., & Herman, J. R. (2006). Deep blue retrievals of Asian aerosol properties during ACE-Asia. *IEEE Transactions on Geoscience and Remote Sensing, 44*, 3180–3195.

IPCC (2007). In S. Solomon, D. Qin, M. Manning, M. Marquis, K. Averyt, M. M. B. Tignor, & H. L. MillerJr. (Eds.), *Climate change 2007 the physical science basis*. Cambridge: Intergovernmental Panel on Climate Change.

Joseph, J. H., & Wiscombe, W. J. (1976). The delta-Eddington approximation for radiative flux transfer. *Journal of the Atmospheric Sciences, 33*, 2452–2459.

Katsev, I. L., Prikhach, A. S., Zege, E. P., Ivanov, A. P., & Kokhanovsky, A. A. (2009). Iterative procedure for retrieval of spectral aerosol optical thickness and surface reflectance from satellite data using fast radiative transfer code and its application to MERIS measurements. In A. A. Kokhanovesky, & G. de Leeuw (Eds.), *Satellite aerosol remote sensing over land* (pp. 101–133). Chichester, UK: Praxis Publishing.

Kaufman, Y. J., & Sendra, C. (1988). Algorithm for automatic atmospheric corrections to visible and Near-IR satellite imagery. *International Journal of Remote Sensing, 9*, 1357–1381.

Kaufman, Y. J., Tanré, D., Gordon, H. R., Nakajima, T., Lenoble, J., Frouin, R., et al. (1997). Passive remote sensing of tropospheric aerosol and atmospheric correction for the aerosol effect. *Journal of Geophysical Research, 102*, 16815–16830.

Kaufman, Y. J., Wald, A. E., Remer, L. A., Gao, B. -C., Li, R. -R., & Luke, F. (1997). The MODIS 2.1-μm channel-correlation with visible reflectance for use in remote sensing of aerosol. *IEEE Transactions on Geoscience and Remote Sensing, 35*, 1286–1298.

King, M. D., & Byrne, D. M. (1976). Method for inferring total ozone content from spectral variation of total optical depth obtained with a solar radiometer. *Journal of the Atmospheric Sciences, 33*, 2242–2251.

Knapp, K. R., Frouin, R., Kondragunta, S., & Prados, A. (2005). Toward aerosol optical depth retrievals over land from GOES visible radiances: Determining surface reflectance. *International Journal of Remote Sensing, 26*, 4097–4116.

Knapp, K. R., Vonder Haar, T. H., & Kaufman, Y. J. (2002). Aerosol optical depth retrieval from GOES-8: Uncertainty study and retrieval validation over South America. *Journal of Geophysical Research-Atmospheres, 107*, D7–D8. http://dx.doi.org/10.1029/2001JD000505.

Kokhanovsky, A. A., & de Leeuw, Gerrit (2009). *Satellite aerosol remote sensing over land* (pp. 1–5). Chichester, UK: Praxis Publshing Ltd.

Lacis, A. A., & Hansen, J. E. (1974). A parameterization for the absorption of solar radiation in the Earth's atmosphere. *Journal of the Atmospheric Sciences, 31*, 118–133.

Leckner, B. (1978). The spectral distribution of solar radiation at the Earth's surface-elements of a model. *Solar Energy*, *20*, 143–150.

Lee, S. S. (2011). Atmospheric science: Aerosols, clouds and climate. *Nature Geoscience*, *4*, 826–827.

Lee, K., & Kim, Y. (2010). Satellite remote sensing of Asian aerosols: A case study of clean, polluted, and Asian dust storm days. *Atmospheric Measurement Techniques*, *3*, 1771–1784.

Levy, R. C., Remer, L. A., & Dubovik, O. (2007). Global aerosol optical properties and application to Moderate Resolution Imaging Spectroradiometer aerosol retrieval over land. *Journal of Geophysical Research-Atmospheres*, *112*, D13210. http://dx.doi.org/10.1029/2006JD007815.

Levy, R. C., Remer, L. A., Mattoo, S., Vermote, E. F., & Kaufman, Y. J. (2007). Second-generation operational algorithm: Retrieval of aerosol properties over land from inversion of moderate resolution imaging spectroradiometer spectral reflectance. *Journal of Geophysical Research-Atmospheres*, *112*, D13211. http://dx.doi.org/10.1029/2006jd007811.

Li, Z., Niu, F., Fan, J., Liu, Y., Daniel, R., & Ding, Y. (2011). Long-term impacts of aerosols on the vertical development of clouds and precipitation. *Nature Geoscience*, *4*, 888–894.

Liang, S. (2000). *Quantitative remote sensing of land surfaces* (pp. 35–36). Hoboken, New Jersey, USA: John Wiley & Sons, Inc.

Liang, S., & Strahler, A. H. (1993). An analytic BRDF model of canopy radiative transfer and its inversion. *IEEE Transactions on Geoscience and Remote Sensing*, *31*, 1081–1092.

Liang, S. L., & Strahler, A. H. (1994). Retrieval of surface BRDF from multiangle remotely sensed data. *Remote Sensing of Environment*, *50*, 18–30.

Liou, K. N. (2002). *An introduction to atmospheric radiation* (pp. 304–305). San Diego, California, USA: Academic Press.

Lyapustin, A., Martonchik, J., Wang, Y., Laszlo, I., & Korkin, S. (2011). Multiangle implementation of atmospheric correction (MAIAC): 1. Radiative transfer basis and look-up tables. *Journal of Geophysical Research-Atmospheres*, *116*, D03210. http://dx.doi.org/10.1029/2010JD014985.

Lyapustin, A., Wang, Y., Laszlo, I., Kahn, R., Korkin, S., Remer, L., et al. (2011). Multiangle implementation of atmospheric correction (MAIAC): 2. Aerosol algorithm. *Journal of Geophysical Research-Atmospheres*, *116*, D03211. http://dx.doi.org/10.1029/2010JD014986.

Meador, W. E., & Weaver, W. R. (1980). Two-stream approximations to radiative transfer in planetary atmospheres — A unified description of existing methods and a new improvement. *Journal of the Atmospheric Sciences*, *37*, 630–643.

Mie, G. (1908). Articles on the optical characteristics of turbid tubes, especially colloidal metal solutions. *Annalen der Physik*, *25*, 377–445.

Molineaux, B., Royer, A., & O'Neill, N. (1998). Retrieval of Pinatubo aerosol optical depth and surface bidirectional reflectance from six years of AVHRR global vegetation index data over boreal forests. *Journal of Geophysical Research-Atmospheres*, *103*, 1847–1856.

Omar, A. H., Won, J. G., Winker, D. M., Yoon, S. C., Dubovik, O., & McCormick, M. P. (2005). Development of global aerosol models using cluster analysis of Aerosol Robotic Network (AERONET) measurements. *Journal of Geophysical Research-Atmospheres*, *110*, D10S14. http://dx.doi.org/10.1029/2004JD004874.

Press, W. H., Teukolsky, S. A., Vetterling, W. T., & Flannery, B. P. (1992). *Numerical recipes in C: The art of scientific computing* (pp. 389–392). Cambridge, UK: Cambridge University Press.

Rahman, H., Pinty, B., & Verstraete, M. M. (1993). Coupled surface-atmosphere reflectance (CSAR) model. 1. Model description and inversion on synthetic data. *Journal of Geophysical Research*, *98*, 20791–20801.

Riffler, M., Popp, C., Hauser, A., Fontana, F., & Wunderle, S. (2010). Validation of a modified AVHRR aerosol optical depth retrieval algorithm over Central Europe. *Atmospheric Measurement Techniques*, *3*, 1255–1270.

Robel, J. (2009). NOAA KLM user's guide with NOAA-N, -N′ supplement. Available online: http://www.ncdc.noaa.gov/oa/pod-guide/ncdc/docs/klm/index.htm (11/30/2011).

Schaaf, C. B., Gao, F., Strahler, A. H., Lucht, W., Li, X., Tsang, T., et al. (2002). First operational BRDF, albedo and nadir reflectance products from MODIS. *Remote Sensing of Environment*, *83*, 135–148.

Seidel, F. C., Kokhanovsky, A. A., & Schaepman, M. E. (2010). Fast and simple model for atmospheric radiative transfer. *Atmospheric Measurement Techniques*, *3*, 1129–1141.

Soufflet, V., Tanre, D., Royer, A., & Oneill, N. T. (1997). Remote sensing of aerosols over boreal forest and lake water from AVHRR data. *Remote Sensing of Environment*, *60*, 22–34.

Stedman, J. R. (2004). The predicted number of air pollution related deaths in the UK during the August 2003 heatwave. *Atmospheric Environment*, *38*, 1087–1090.

Stowe, L. L., Davis, P. A., & McClain, E. P. (1999). Scientific basis and initial evaluation of the CLAVR-1 global clear cloud classification algorithm for the advanced very high resolution radiometer. *Journal of Atmospheric and Oceanic Technology*, *16*, 656–681.

Stowe, L. L., McClain, E. P., Carey, R., Pellegrino, P., Gutman, G. G., Davis, P., et al. (1991). Global distribution of cloud cover derived from NOAA/AVHRR operational satellite data. *Advances in Space Research*, *11*, 51–54.

Strahler, A. H. (1999). *MODIS land cover and land-cover change product: Algorithm theoretical basis document (ATBD) version 5.0.*

Strahler, A. H., & Muller, J. -P. (1999). *MODIS BRDF/albedo product: Algorithm theoretical basis document (ATBD) version 5.0.*

Tanré, D., Deschamps, P. Y., Devaux, C., & Herman, M. (1988). Estimation of Saharan aerosol optical thickness from blurring effects in Thematic Mapper data. *Journal of Geographical Research*, *93*, 15955–15964.

Veefkind, J. P., de Leeuw, G., & Durkee, P. A. (1998). Retrieval of aerosol optical depth over land using two-angle view satellite radiometry during TARFOX. *Geophysical Research Letters*, *25*, 3135–3138.

Verstraete, M., Pinty, B., & Dickinson, R. E. (1990). A physical model of the bidirectional reflectance of vegetation canopies. 1. Theory. *Journal of Geophysical Research*, *95*, 11755–11765.

von Hoyningen-Huene, W., Freitag, M., & Burrows, J. B. (2003). Retrieval of aerosol optical thickness over land surfaces from top-of-atmosphere radiance. *Journal of Geophysical Research-Atmospheres*, *108*, D9. http://dx.doi.org/10.1029/2001JD002018.

von Hoyningen-Huene, W., Yoon, J., Vountas, M., Istomina, L. G., Rohen, G., Dinter, T., et al. (2011). Retrieval of spectral aerosol optical thickness over land using ocean color sensors MERIS and SeaWiFS. *Atmospheric Measurement Techniques*, *4*, 151–171.

Wagner, S. C., Govaerts, Y. M., & Lattanzio, A. (2010). Joint retrieval of surface reflectance and aerosol optical depth from MSG/SEVIRI observations with an optimal estimation approach: 2. Implementation and evaluation. *Journal of Geophysical Research-Atmospheres*, *115*, D02204. http://dx.doi.org/10.1029/2009JD011780.

Wanner, W., Li, X., & Strahler, A. H. (1995). On the derivation of kernels for kernel-driven models of bidirectional reflectance. *Journal of Geophysical Research-Atmospheres*, *100*, 21077–21089.

Wilson, W. E., Levy, A., & McDonald, E. H. (1972). Role of sulfur dioxide and photochemical aerosol in eye irritation from photochemical smog. *Environmental Science & Technology*, *6*, 423–427.

Xue, Y., & Cracknell, A. P. (1995). Operational bi-angle approach to retrieve the earth surface albedo from AVHRR data in the visible band. *International Journal of Remote Sensing*, *16*, 417–429.

Zhang, H., Lyapustin, A., Wang, Y., Kondragunta, S., Laszlo, I., Ciren, P., et al. (2011). A multi-angle aerosol optical depth retrieval algorithm for geostationary satellite data over the United States. *Atmospheric Measurement Techniques*, *11*, 11977–11991.